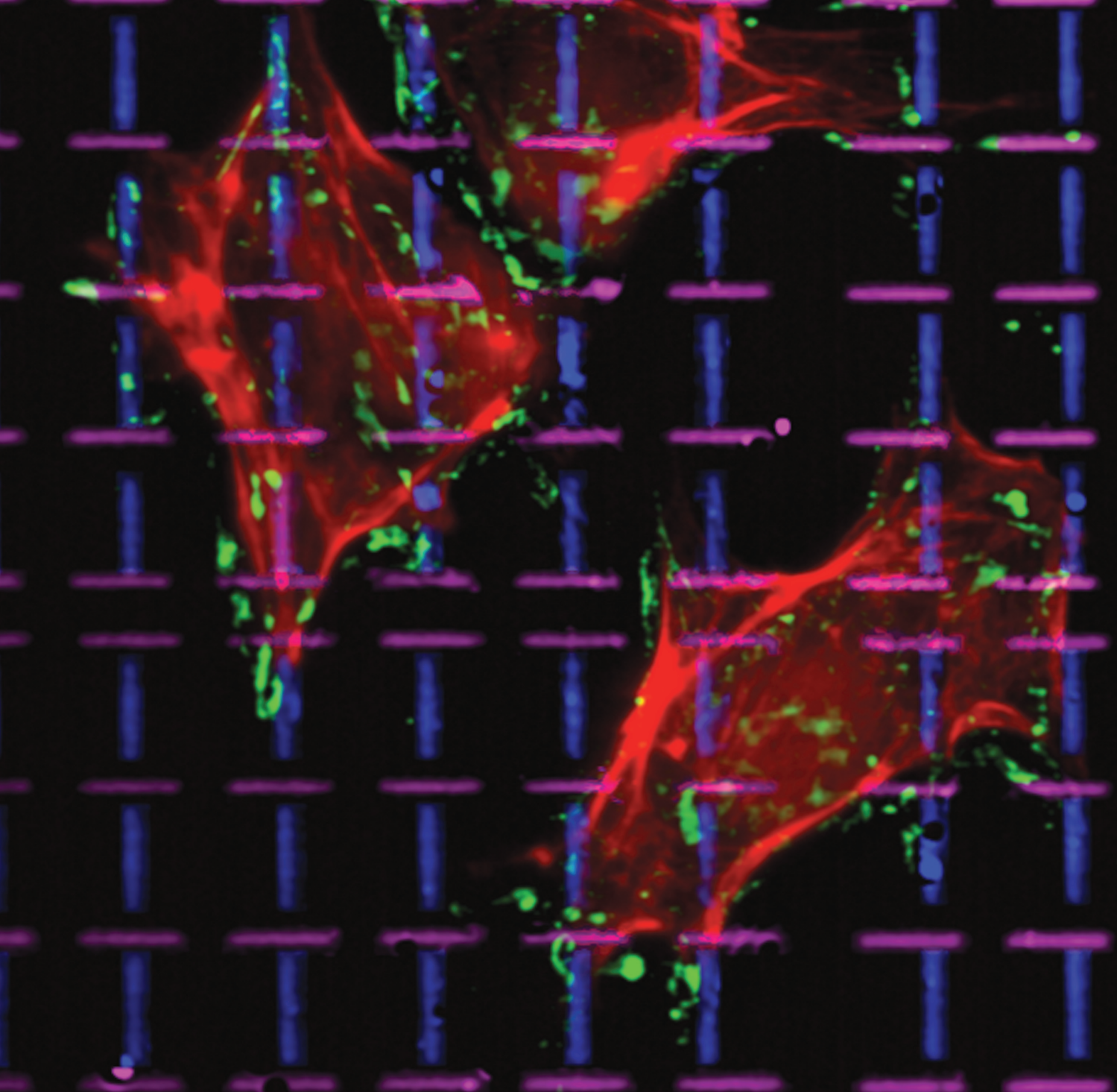


ADVANCED FUNCTIONAL MATERIALS



Fabrication of Multifaceted Micropatterned Surfaces with Laser Scanning Lithography

John H. Slater, Jordan S. Miller, Shann S. Yu, and Jennifer L. West*

The implementation of engineered surfaces presenting micrometer-sized patterns of cell adhesive ligands against a biologically inert background has led to numerous discoveries in fundamental cell biology. While existing surface patterning strategies allow patterning of a single ligand, it is still challenging to fabricate surfaces displaying multiple patterned ligands. To address this issue we implemented laser scanning lithography (LSL), a laser-based thermal desorption technique, to fabricate multifaceted, micropatterned surfaces that display independent arrays of subcellular-sized patterns of multiple adhesive ligands with each ligand confined to its own array. We demonstrate that LSL is a highly versatile “maskless” surface patterning strategy that provides the ability to create patterns with features ranging from 460 nm to 100 μm , topography ranging from -1 to 17 nm, and to fabricate both stepwise and smooth ligand surface density gradients. As validation for their use in cell studies, surfaces presenting orthogonally interwoven arrays of $1 \mu\text{m} \times 8 \mu\text{m}$ elliptical patterns of Gly-Arg-Gly-Asp-terminated alkanethiol self-assembled monolayers and human plasma fibronectin are produced. Human umbilical vein endothelial cells cultured on these multifaceted surfaces form adhesion sites to both ligands simultaneously and utilize both ligands for lamella formation during migration. The ability to create multifaceted, patterned surfaces with tight control over pattern size, spacing, and topography provides a platform to simultaneously investigate the complex interactions of extracellular matrix geometry, biochemistry, and topography on cell adhesion and downstream cell behavior.

1. Introduction

Surfaces displaying patterned arrays of an immobilized biomolecule against an inert background show much promise for use as model substrates to investigate cell–surface interactions^[1,2] and as platforms for biosensors.^[2] Self-assembled monolayers (SAMs) of alkanethiols on gold (Au) are often implemented in the fabrication of patterned surfaces due to the high tailorability of the terminal group functionality. A diverse range of biomolecules including oligonucleotides,^[3] peptides,^[4] and full proteins^[5] have been immobilized with alkanethiol SAMs either through directed adsorption^[5] or terminal end tethering using specific coupling chemistries.^[6] Implementation of patterned

SAM surfaces that restrict the extent of cell spreading or that regulate cytoskeletal tension has led to a number of discoveries including the ability to prevent down regulation of cell function in culture,^[7] to direct lineage-specific stem cell differentiation,^[8,9] and to manipulate cell motility.^[10] An analogous approach to regulate the extent of cytoskeletal tension generation is through engineering cell adhesion site geometry with respect to adhesion site shape, size, or spacing. Geometric regulation of adhesion sites has been used to induce directional cell motility,^[11,12] to direct the organization of intracellular components,^[13] and to induce cellular differentiation.^[14] These examples demonstrate the importance of intracellular force generation on cell function but neglect the influence of chemical cues (matrix composition) on cell behavior.

The extracellular matrix (ECM) is made up of many proteins and polysaccharides^[15] and integrin-mediated adhesion to individual components can influence intracellular signaling cascades governed by adhesion site plaques that dictate cell behavior.^[16] For example, capillary morphogenesis of endothelial cells is observed in cells cultured on collagen I but not in

cells on laminin, indicating matrix-specific guidance of cell behavior.^[17] A better understanding of how ECM composition influences cell fate could be formed with model substrates that allow control over both intracellular force generation and the composition of cellular adhesions through use of multiple ligands. While it is fairly straightforward to create surfaces displaying patterned arrays of a single ligand using existing technologies (e.g., microcontact printing), the fabrication of multifaceted surfaces that present patterned arrays of multiple ligands with each ligand confined to its own array is still quite challenging.

Toward this goal, a few strategies to create multifaceted surfaces have been developed. Variations of microcontact printing including microfluidic inking of PDMS stamps and multilevel stamps have been used to pattern multiple proteins on a single surface^[18–20] or for patterning cells.^[19,20] Microcontact printing of Arg-Gly-Asp-terminated (RGD) SAMs containing electroactive moieties provided a method for cell patterning through site-selective alkanethiol release via an applied potential.^[21]

Dr. J. H. Slater, Dr. J. S. Miller, S. S. Yu, Prof. J. L. West
 Department of Bioengineering Rice University Houston
 Texas 77005, USA
 E-mail: jwest@rice.edu

DOI: 10.1002/adfm.201100297

Light-based techniques that rely on photochemical reactions have also been developed.^[22,23] Alignment of three distinct alkanethiol SAMs was achieved using alkanethiols sensitive to specific wavelengths of light in which Au-S scission occurred at 220 nm and cleavage of an o-nitrobenzyl amine-protecting group at 365 nm.^[22] Light-activated affinity micropatterning was implemented to reveal a caged biotin upon exposure to ultraviolet light, thereby allowing immobilization of biotinylated antibodies in patterned arrays.^[23] While all of the aforementioned patterning strategies allow high resolution patterning,^[24] they have not been implemented to create multifaceted surfaces that display sub-cellular sized arrays of multiple ligands in close proximity due to various limitations associated with each technique. Furthermore, all of these techniques require the fabrication of photolithographic masters to mold a PDMS stamp or to act as a photomask for spatially defined photochemical patterning. Any change in pattern design requires fabrication of a new master.

To circumvent the need for clean room facilities and to provide flexibility in pattern design with little lead time, a few maskless patterning strategies have been developed to create multifaceted surfaces. Dip-pen nanolithography was used to write multiple thiol derivatized oligonucleotides on Au surfaces for the fabrication of DNA sensors.^[25] Doyle et al. developed microphotopatterning, a technique based on photolytic ablation of poly(vinyl alcohol) tethered from silane SAMs to create surfaces displaying multiple patterned proteins.^[10] Although the ability to create multifaceted surfaces was demonstrated, no cell data using these surfaces has been presented.^[10]

Here, we describe the implementation of laser scanning lithography (LSL) for the fabrication of multifaceted surfaces that present two distinct cell adhesive ligands in patterned arrays against a biologically inert background. Laser induced thermal desorption of an alkanethiol SAM was first introduced in 1993 for the fabrication of mixed thiol SAMs.^[26] Since then it has been refined and used to fabricate surfaces presenting two alkanethiol SAMs with different wettabilities,^[27,28] to pattern chemical gradients of two SAMs,^[29] and to pattern three different SAMs in close proximity on a single surface.^[30] In general, the technique involves functionalizing a Au surface with an alkanethiol SAM of choice. A focused laser beam is used to remove desired patterns of the SAM through thermally induced alkanethiol desorption. The laser energy absorbed by the Au film is released as heat thereby inducing a highly localized increase in surface temperature. At 212 °C, the SAM is desorbed from the surface via disulfide bond formation between adjacent thiols^[27] and the bare Au patterns are backfilled with a second alkanethiol of choice. Successive cycles of the process can be used to pattern multiple alkanethiol SAMs in close proximity with high spatial resolution on a single surface.

Here, we demonstrate the use of LSL to create multifaceted, patterned surfaces that display arrays of subcellular-sized patterns of two cell adhesive ligands; human plasma fibronectin (HFN) and the integrin ligating peptide RGD derived from FN. We show that thermally-induced alkanethiol SAM desorption occurs through Au-S scission, pattern size can be finely tuned through careful manipulation of the laser and substrate properties, patterns with controlled nanotopography can be created, and patterns as small as 460 nm (0.17 μm²) can be created, and

sub-diffraction limited patterning is possible. Furthermore we demonstrate that cells cultured on multifaceted surfaces displaying interwoven patterns of a GRGD-terminated SAM and HFN bind concurrently to the two adhesive ligands and utilize both patterned ligands during migration.

2. Results and Discussion

2.1. Fabrication of Multifaceted Surfaces with LSL

The LSL fabrication process is schematically outlined in Figure 1A. A Au-coated glass coverslip is functionalized with an alkanethiol of choice to create the first SAM. A 532 nm laser is focused on the Au surface through a 20× (NA0.8) air or 63× (NA1.4) oil immersion objective and raster scanned in desired regions of interest (ROIs) to thermally desorb patterns of the first SAM in a N₂-rich atmosphere. A second SAM is formed on the bare Au patterned regions. Successive cycles of this process allow the fabrication of multifaceted surfaces: surfaces that display multiple chemical functionalities with each functionality confined to its own patterned array.

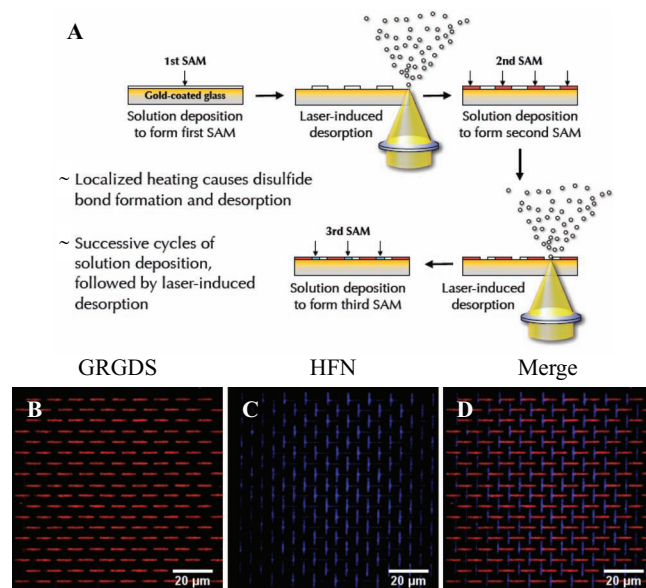


Figure 1. Schematic of the LSL Process to Create Multifaceted Patterned Surfaces. A) A Au-coated glass coverslip is functionalized with an OEG-terminated alkanethiol. Desired regions of the OEG SAM are thermally desorbed from the surface with a 532 nm laser. The patterned bare Au regions are exposed to a second alkanethiol. Successive cycles of the process allow patterning of multiple SAMs or biomolecules in close proximity. B–D) A multifaceted surface created with LSL displaying independent arrays of two cell adhesive ligands, B) GRGDS and C) HFN. B) An OEG SAM was formed on a Au surface and an array of 1 μm × 8 μm ellipses of the OEG was thermally desorbed with a 532 nm laser. The bare Au patterned regions were functionalized with a GRGDS-terminated alkanethiol and fluorescently labeled. C) A second round of patterning, orthogonal to the GRGDS patterns, was performed and exposed to fluorescently labeled HFN. D) The multifaceted surface displays independent arrays of GRGDS (red horizontal patterns) and HFN (blue vertical patterns) against a passive background. B–D) SB = 20 μm.

A multifaceted surface displaying two patterned cell adhesive ligands against a biologically inert background is displayed in Figure 1D. A Au surface was functionalized with a 2 mM ethanolic solution of $\text{HS}(\text{CH}_2)_{15}\text{CONHCH}_2\text{CH}_2(\text{OCH}_2\text{CH}_2)_5\text{OH}$ (OEG) for 1 h to create a protein repulsive and biologically inert background. An array of $1 \mu\text{m} \times 8 \mu\text{m}$ ellipses of the OEG SAM was thermally desorbed with a 532 nm laser focused through a $20\times$ (NA0.8) objective operating at a fluence of $12.80 \text{ nJ } \mu\text{m}^{-2}$. The resulting bare Au patterns were functionalized with a 2 mM ethanolic solution of $\text{HS}(\text{CH}_2)_{15}\text{CONHCH}_2\text{CH}_2(\text{OCH}_2\text{CH}_2)_{11}\text{-GRGDS}$ (GRGDS) for 1 h and the peptide fluorescently labeled (Figure 1B). A second set of ROIs, orthogonal to the first, of the OEG SAM was desorbed and the patterns exposed to fluorescently labeled HFN ($12.5 \mu\text{g mL}^{-1}$ in PBS for 30 min at 37°C) (Figure 1C). The multifaceted surface presents two distinct cell adhesive ligands (full length HFN (Figure 1C) and the peptide sequence RGD derived from the FN-III10 domain (Figure 1B)) in defined patterned arrays with each ligand confined to its own array against a biologically inert background (Figure 1D). While both HFN and RGD support the formation of cellular adhesion sites, HFN contains additional integrin ligating domains and can undergo fibrillogenesis. Cell studies with multifaceted surfaces that display these two patterned ligands allow the simultaneous investigation of the influences of biophysical (ECM geometry) and biochemical cues (integrin ligation) on cell behavior. Although cell adhesive ligands were patterned in this study, the LSL fabrication process allows patterning of multiple biomolecules of choice either through conjugation to or tethering from alkanethiol SAMs or through adsorption to bare Au or alkanethiol functionalized patterns.

2.2. Design Rationale and Verification of Selective SAM Desorption

Previous studies using laser-assisted thermal desorption of alkanethiol SAMs implemented a continuous-wave 488 nm laser to pattern 30 nm Au films^[27,29,31] or a pulsed 532 nm laser to pattern 300 nm Au films.^[28,30] In this study, thin ($\leq 10 \text{ nm}$) Au films were patterned with a continuous-wave 532 nm laser for two reasons: i) thin ($\leq 20 \text{ nm}$) Au films are optically semi-transparent allowing fluorescent microscopy to be implemented for pattern characterization and microscopic evaluation of cells and ii) so that low laser energy (short irradiation time) could be used for patterning. Thin ($< 15 \text{ nm}$) Au films display a peak in their extinction spectra dominated by high absorption from 520–560 nm^[32,33] that coincides with the formation of surface plasmons^[33] that decay as heat. Au films display a minimum in their extinction spectra from 460–500 nm.^[32,33] As a consequence, the absorption of Au films can be $\sim 2\times$ higher at 532 nm compared to 488 nm.^[32] Au films also exhibit decreased in-plane thermal conductivity with decreased film thickness.^[34] The conductivity can diminish by a factor of $\sim 2\times$

when the thickness decreases from 30 to 6 nm as a result of changes in grain morphology.^[34] Laser-induced thermal desorption of SAMs occurs when the energy of the light adsorbed by the Au film is released as heat resulting in a highly localized increase in surface temperature in the irradiated region.^[27,35] Approximately 50% of the SAM is removed at a surface temperature of 160°C ^[36] with complete desorption occurring at $210\text{--}212^\circ\text{C}$.^[27,36] Since LSL is a thermal-based process one would anticipate more efficient patterning (heat generation) to occur at a wavelength with higher absorption (532 nm compared to 488 nm) and when thinner Au films with decreased thermal conductivity are employed. For comparison, Iversen et al. implemented a continuous-wave 488 nm laser operating at 6 mW (42 mW μm^{-2} as calculated from Eq. 2) focused through a $100\times$ (NA1.4) objective with irradiation times of 60–210 s to pattern 30 nm Au substrates.^[31] In the work presented here, patterning of 10 nm Au films was achieved with a 532 nm laser operating at 3.5 mW ($\sim 21 \text{ mW } \mu\text{m}^{-2}$) focused through a $63\times$ (NA1.4) objective with an exposure time as low as 0.95 μsec ; the highest exposure time was 63.9 msec when operating with a pixel dwell time of 6.39 μsec and 10 000 iterations per ROI. This comparison suggests that patterning at wavelengths that lie in the high absorption regime combined with the use of ultrathin Au films that have higher thermal resistivity allows more efficient patterning. The increased efficiency allows patterning at lower laser fluence (highly reduced exposure time) making the process drastically faster.

Laser-assisted thermally-induced SAM desorption from Au surfaces has been confirmed by secondary ion mass spectroscopy,^[29] cyclic voltammetry,^[30] condensation,^[27–29] scanning electron microscopy,^[27,30,31,35] fluorescence,^[28] and atomic^[31] or lateral force microscopies.^[28] In this study, surface mapping X-ray photoelectron spectroscopy (XPS) was implemented to verify laser-induced thermal desorption of an OEG SAM in the patterned ROIs through analysis of the C_{1s}, O_{1s}, and S_{2p} spectra to monitor the presence of the alkyl chain, oligo(ethylene glycol) terminal group, and thiol head group respectively. A 4×4 array of star-shaped ROIs with a characteristic length of 100 μm was used to thermally desorb an OEG SAM. The C_{1s}, O_{1s}, and S_{2p} spectra were mapped using a 9 μm X-ray spot size. Figure 2 demonstrates that the C_{1s}, O_{1s}, and S_{2p} signal intensities of the OEG SAM were void in the star-shaped patterned

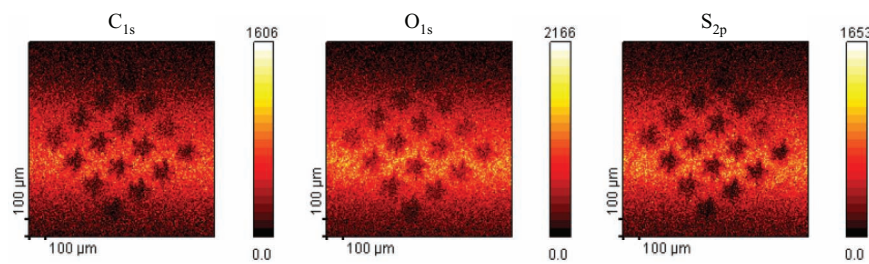


Figure 2. Verification of Alkanethiol Desorption. A 4×4 array of star-shaped patterns with a characteristic length of 100 μm was used to thermally desorb an OEG SAM with a 532 nm laser. The patterned surface was imaged via map scanning XPS. The C_{1s}, O_{1s}, and S_{2p} spectra were attained to monitor the removal of the alkyl chain, OEG terminal group, and thiol head group respectively. Absence of signal in the patterned regions in the S_{2p} spectra indicates thermally induced desorption of the OEG SAM through Au-S scission. The background gradient is due to spherical aberration from the X-ray positioning system. SB = 100 μm .

regions while the surrounding OEG background maintained high signal intensities in all spectra. The results confirm site specific thermal desorption of the alkanethiol SAM upon localized heating. The absence of signal in the patterned regions in the S_{2p} spectra indicates SAM desorption through Au-S scission.^[22,27] Au-S scission is a crucial step in providing clean Au patterns that allow further functionalization when exposed to subsequent SAMs. If thiol residues remain on the surface, further functionalization steps could be inhibited.

2.3. Controlling Pattern Feature Size

LSL is a thermal-based desorption technique that relies on localized heating. Due to the thermal nature of the process the pattern feature size can be tuned by refining the: i) amount of energy delivered to the Au film, ii) wavelength used for patterning, iii) beam waist of the focused laser, iv) numerical aperture of the objective, v) optical properties (absorption) of the Au film, vi) thermal properties (conductivity) of the Au film, and vii) activation energy needed for SAM desorption. In these studies, the influences of laser fluence, number of passes per ROI, Au film thickness (conductivity), and objective NA on pattern size were systematically investigated. Tight control over pattern feature size and the ability to create nano- to micrometer-sized patterns is demonstrated through fine tuning of these parameters.

2.3.1. Influence of Laser Patterning Parameters (Fluence and Iterations) on Pattern Feature Size

To gain a better understanding of the relationship between the amount of energy delivered to the Au film and the resulting pattern size, arrays of 1×20 pixel ROIs of an OEG SAM were desorbed with systematic variations in the laser fluence and number of iterations per ROI (Figure 3). 10 nm Au films were functionalized with OEG, 1×20 pixel ROIs of the OEG SAM were thermally desorbed, the surfaces exposed to HFN (12.5 $\mu\text{g mL}^{-1}$ in PBS for 30 min at 37 °C), the HFN fluorescently labeled, the resulting patterns imaged via fluorescent microscopy, and the patterned regions mathematically fit with ellipses to characterize the minor axis and area of the patterns for each condition. 1 pixel wide ROIs were implemented so that the minor axis of the ellipses, which corresponds to the Airy Disk of the focused laser beam, was indicative of the minimum feature size achievable. Noticeable increases in pattern size were only observed in the minor axis (1 pixel wide, perpendicular to scanning direction) and not the major axis (20 pixels long, parallel to scanning direction). Deviation in the size of the major axis was large enough to shield any elongation in pattern length induced by changing the laser parameters therefore linear increases in both the minor axis and pattern

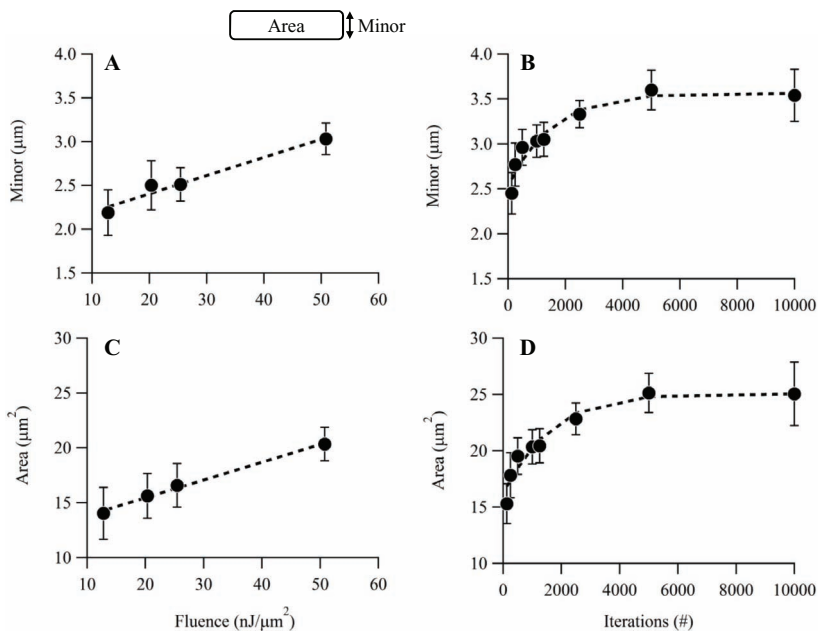


Figure 3. Influence of Laser Fluence and Iterations on Pattern Size. 10 nm Au films were functionalized with an OEG-terminated alkanethiol and arrays of 1×20 pixel ROIs of the SAM were thermally desorbed with a 532 nm laser focused through a 20× (NA0.8) objective with varying laser fluence (12.8–50.8 $\text{nJ}/\mu\text{m}^2$) and number of iterations (125–10 000) per ROI. The patterned surfaces were exposed to HFN, the HFN patterns mathematically fit with ellipses, and the (A,B) minor axis and (C,D) area measured for each set of patterning conditions. The (A) minor axis and (C) area displayed a linear increase with increased laser fluence at a constant number of iterations (1000) per ROI. The (B) minor axis and (D) pattern area increased with increased iterations at a constant fluence (50.8 $\text{nJ}/\mu\text{m}^2$) that plateaued at ~5000 iterations.

area with increased laser fluence were observed (Figure 3A, C). The minor axis linearly increased with increased laser fluence at a constant number of iterations (Figure 3A) as reported by others.^[27,31,35] When patterning over a fluence range of 12.80–50.80 $\text{nJ}/\mu\text{m}^2$ with a constant 1000 iterations per ROI, the minor axis increased from 2.19 ± 0.26 to $3.03 \pm 0.18 \mu\text{m}$ (Figure 3A). The pattern area displayed the same trend and increased from 14.04 ± 2.37 to $20.34 \pm 1.52 \mu\text{m}^2$ (Figure 3C).

The influence of repeated passes on feature size was also investigated and a sigmoidal relationship was observed (Figure 3B,D). The minor axis of the elliptical patterns increased from $2.45 \pm 0.23 \mu\text{m}$ at 125 iterations that began to plateau at ~5000 iterations at $3.60 \pm 0.22 \mu\text{m}$ when patterning with a constant fluence of $50.8 \text{ nJ}/\mu\text{m}^2$ (Figure 3B). The area of the elliptical patterns followed the same trend and increased from 15.29 ± 1.76 to $25.13 \pm 1.73 \mu\text{m}^2$ over the same range of iterations (Figure 3D). As more energy was delivered to the Au film by increasing the fluence or number of passes, more heat was generated. With highly conductive films, this resulted in enlarging of the spatial region that reached the crucial temperature (212 °C) for thermally-induced SAM desorption resulting in larger patterns.

2.3.2. Au Film Thickness (Conductivity) Influence on Pattern Feature Size

The in-plane thermal conductivity of thin Au films is a function of film thickness, and the conductivity can more than

double when the film thickness increases from 6 to 30 nm as a consequence of changes in film morphology and structure.^[34] Since LSL relies on localized heating, the influence of Au film thickness was investigated as a means to control pattern size. Given that the thermal conductivity decreases in thinner Au films, one would expect smaller patterns to be formed due to increased heat confinement to the irradiated region. Additionally, since thinner films have higher thermal resistivity, the local surface temperature should increase more rapidly allowing patterning at lower laser energy. To test this idea, 1 × 20 pixel ROIs were patterned on 6, 8, and 10 nm Au films with systematic variations in the laser fluence and number of iterations per ROI and the resulting patterns characterized as described in Section 2.3.1. Three-dimensional graphs of the pattern minor axis (Figure 4A-C) and area (Figure 4D-F) as a function of laser fluence and number of iterations were created. The same trends of increased pattern size with increased fluence at a constant number of iterations and vice versa were observed as discussed in Section 2.3.1. A trend of increased

feature size with increased Au film thickness was also observed (Figure 4). As expected with a thermal process, the largest features (2.13, 3.06, and 3.60 μm for the 6, 8, and 10 nm surfaces respectively) were formed when the most energy was delivered to the Au, i.e., at the highest fluence (50.80 nJ μm⁻²) and number of iterations (10 000) (Figure 4A-C). Conversely, the smallest features (1.33, 1.38, and 1.48 μm for the 6, 8, and 10 nm surfaces respectively) were created at the lowest fluence (12.8 nJ μm⁻²) and least number of iterations (125) (Figure 4 A-C). It should be noted that a minimum fluence of ~10–12 nJ μm⁻² was needed to thermally desorb some of the OEG SAM when operating at a low number of iterations (1 or 10) using 10 nm Au films. 10 nm Au films displayed the highest flexibility in pattern size as a function of the patterning parameters (Figure 4A,D) followed by the 8 nm (Figure 4B,E) and then the 6 nm (Figure 4C,F) Au films. These results indicate that the thickness of the Au film plays a significant role in controlling pattern feature size which most likely emanates from differences in the thermal conductivity of the Au films. The

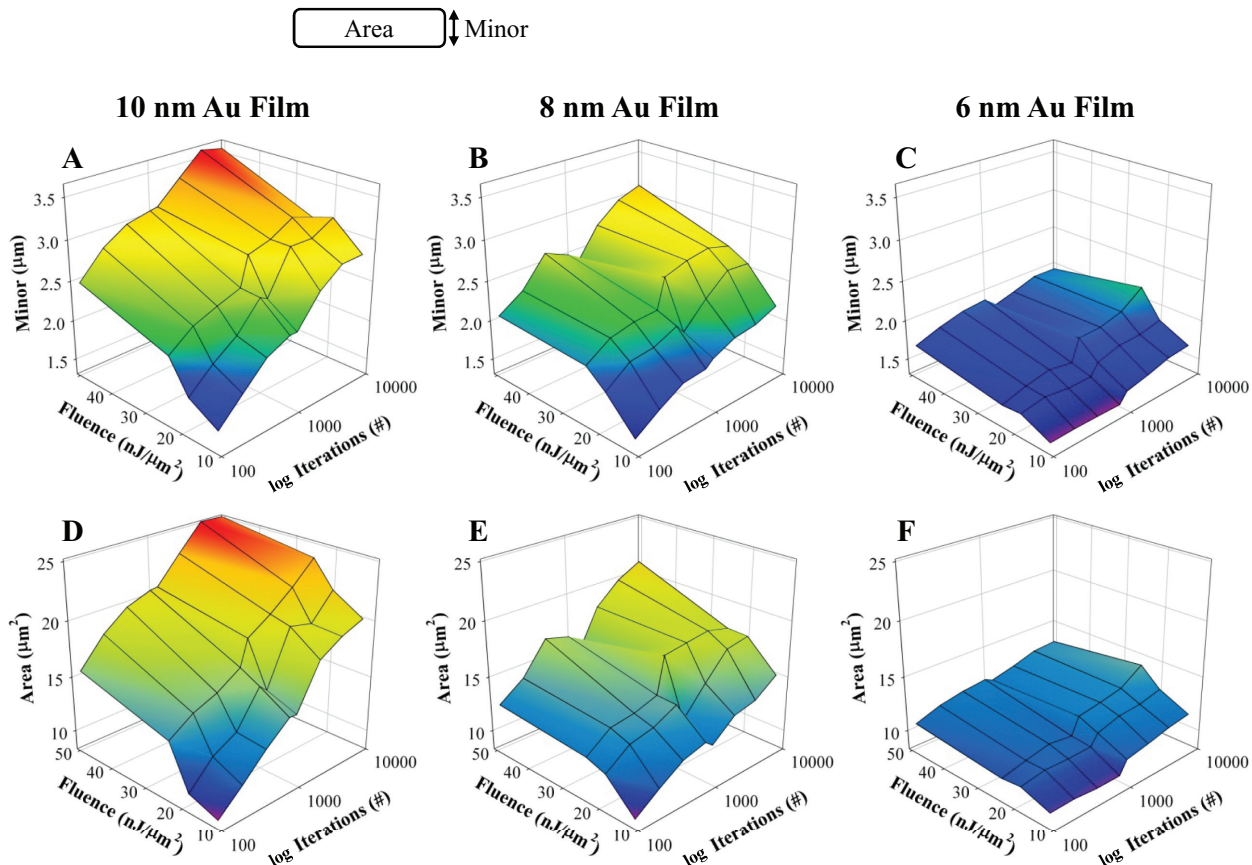


Figure 4. Tuning Pattern Size by Varying Laser Fluence, Iterations, and Au Film Thickness. 3D plots displaying the measured pattern (A–C) minor axis and (D–F) area as a function of laser fluence and number of iterations per ROI for elliptical patterns created on (left column) 10, (middle column) 8, and (right column) 6 nm thick Au films. Au films with the indicated thickness were functionalized with an OEG-terminated alkanethiol and arrays of 1 × 20 pixel ROIs of the OEG SAM were thermally desorbed from the surface with a 532 nm laser focused through a 20× (NA 0.8) objective with varying laser fluence (12.8–50.8 nJ μm⁻²) and number of iterations (125–10 000) per ROI. The (A–C) minor axis and (D–F) area of the HFN patterns were measured for each set of patterning conditions. Pattern enlarging was observed on all of the Au films as a function of both increased laser fluence and number of iterations. As the thermal conductivity of the Au film was decreased by reducing the film thickness, the extent of pattern enlarging was reduced. Due to the thermal nature of the LSL process, pattern size can be finely tuned through optimization of the energy input into the substrate and the substrate thermal properties.

ability to generate a large range of pattern sizes by increasing the amount of energy delivered to the film was suppressed on 6 nm films (Figure 4C,F). Due to the high thermal resistivity of these surfaces, delivery of increased energy resulted in melting of the Au layer and the formation of topographical features rather than spreading of the heat and pattern enlarging as observed on 8 and 10 nm Au substrates.

2.3.3. Patterns with Controlled Topography

Cells possess the ability to sense and respond to the topography of the underlying substrate and surfaces with varying levels of nanotopography have been implemented to induce changes in cell function.^[37] We tested the ability to precisely modulate the extent of topography created in the patterned regions by tuning the laser and Au film parameters used for LSL patterning. Two distinct mechanisms of thermally-induced alkanethiol SAM desorption from Au surfaces have been demonstrated and are termed non-specific and chemically-specific patterning.^[31] Non-specific patterning occurs when thin layers of the Au film are vaporized from the surface in the region of the focused laser beam. This mode of patterning removes the Au and SAM concurrently, resulting in 1–11 nm indentations in the irradiated, patterned regions depending on the laser energy delivered to the film.^[31] Chemically-specific patterning occurs in the absence of Au film vaporization where only the SAM is desorbed, resulting in topography-free, purely chemical patterns.^[31] These two modes of patterning are surface temperature dependent where chemically-specific patterning occurs at low laser energy (low surface temperature, 212 °C) while non-specific patterning occurs at higher energy (high surface temperatures, 1064 °C).^[31] The work presented here adds a third mode of laser induced thermal patterning we have termed “topographical patterning” in which ultrathin (6 nm) Au surfaces undergo hydrodynamic melting rather than vaporization, resulting in patterns with raised topography of controlled height on the nanometer scale.

Two modes of laser-induced thermal ablation of thin Au films have been described, vaporization and hydrodynamic ablation.^[38] During vaporization, thin layers of the Au film are evaporated from the surface resulting in indentations in the irradiated regions. In hydrodynamic ablation, the Au melts, coalesces to form ridges, and is eventually ejected from the surface as droplets upon reaching a crucial size resulting in the formation of raised topographical features.^[38,39] Figure 4C,F demonstrates that patterns created on 6 nm Au surfaces do not enlarge as drastically with increased energy input as patterns created on thicker 8 (Figure 4B,E) and 10 nm (Figure 4A,D) Au films. To gain insight into this occurrence we examined the topography of patterned surfaces using white light interferometry.

While both chemically-specific and non-specific patterning were observed on 6 and 10 nm thick Au films (Figure 5), a third regime of patterning that resulted in raised topographical features was observed only on 6 nm Au films (Figure 5 A–C). Patterns created with the highest fluence (50.8 nJ μm⁻²) and number of iterations (10 000) displayed ~1 nm dips on 10 nm Au films (Figure 5D). As the energy delivered to the film was steadily decreased by lowering the fluence and number of iterations, the

dips reduced to <0.5 nm, indicating a shift from non-specific to chemically-specific patterning (Figure 5 D–F). A similar occurrence was observed on 6 nm Au films where ~0.5 nm dips were measured in patterns created with an intermediate fluence (25.4 nJ μm⁻²) and 1 iteration (Figure 5B) while flat regions were observed at lower fluence (12.8 nJ μm⁻²) and ≤10 iterations (Figure 5C). Above these energy thresholds a third mode of patterning was observed in which the irradiated regions of the Au underwent hydrodynamic melting instead of vaporization. Topographical patterning occurred on 6 nm films when ≥10 iterations were used at fluences of 50.8 (Figure 5A) or 25.4 nJ μm⁻² (Figure 5B) or when ≥100 iterations were implemented at 12.8 nJ μm⁻² (Figure 5C). Figure 5A–C shows that the extent of the topography in the patterned regions can be tuned by controlling the amount of energy delivered to the film. When patterning with a fluence of 50.8 nJ μm⁻², the topography decreased from ~17 nm at 10 000 iterations to ~0.5 nm at 1 iteration (Figure 5A). The same trend was observed in Figure 5B,C where increased energy input resulted in increased surface topography.

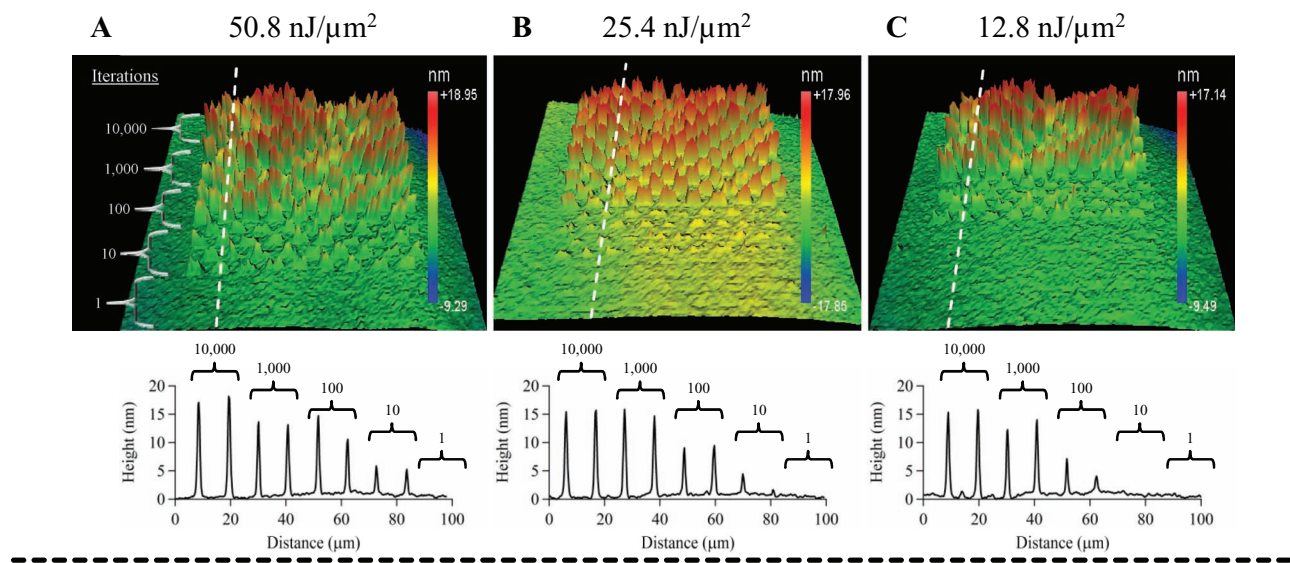
2.3.4. Nano- and Sub-Diffraction Limited Patterning with LSL

Cells adhere to ECM proteins through integrin-mediated adhesions^[40] that mature from small (<0.25 μm²) nascent adhesions to larger (>1 μm²) focal adhesions.^[41–43] Each stage of maturation involves inclusion of various intracellular signaling motifs that govern many aspects of cell behavior.^[44] Direct control over adhesion site size using surfaces presenting micro-^[14] or nanopatterns^[45] of adhesive ligands has been implemented to influence cytoskeleton formation,^[14] spreading,^[45] and proliferation.^[45] In order to manipulate intracellular signaling cascades regulated by adhesion sites, it would be advantageous to gain control over adhesion maturation by limiting adhesion site growth. The feasibility of using LSL to create patterns in this size regime was tested.

The size of the patterns created with LSL can be minimized by using: i) a high NA objective, ii) low laser fluence and few iterations to minimize heat generation, and iii) thin Au films with decreased thermal conductivity to prevent lateral spreading of the generated heat and subsequent pattern enlarging. 1 × 1 (smaller circular patterns in Figure 6A,B) and 1 × 3 (larger oval patterns in Figure 6A,B) pixel ROIs of HFN were patterned on a 10 nm Au film with a 532 nm laser operating at a fluence of 33.38 nJ μm⁻² focused through a 63× (NA 1.4) oil immersion objective with varying iterations per ROI. The sigmoidal relationship between pattern size and the number of iterations as described in Section 2.3.1 was observed (Figure 6C,D). The diameter of the small circular patterns increased from 460 ± 100 nm (0.17 ± 0.07 μm²) at 100 iterations to 1.07 ± 0.03 μm (0.90 ± 0.05 μm²) at 10 000 iterations. The minimum feature size (460 nm) correlates well with the diameter of the Airy Disk (464 nm).

Since laser-assisted SAM desorption is a photothermal process rather than a photochemical process, we hypothesized that sub-diffraction limited patterns could be created through minimization of the laser fluence and substrate conductivity. Shadnam et al. created a model based on experimental data

Patterns with Raised Topography 6 nm Au Films



Patterns with Indented Topography 10 nm Au Films

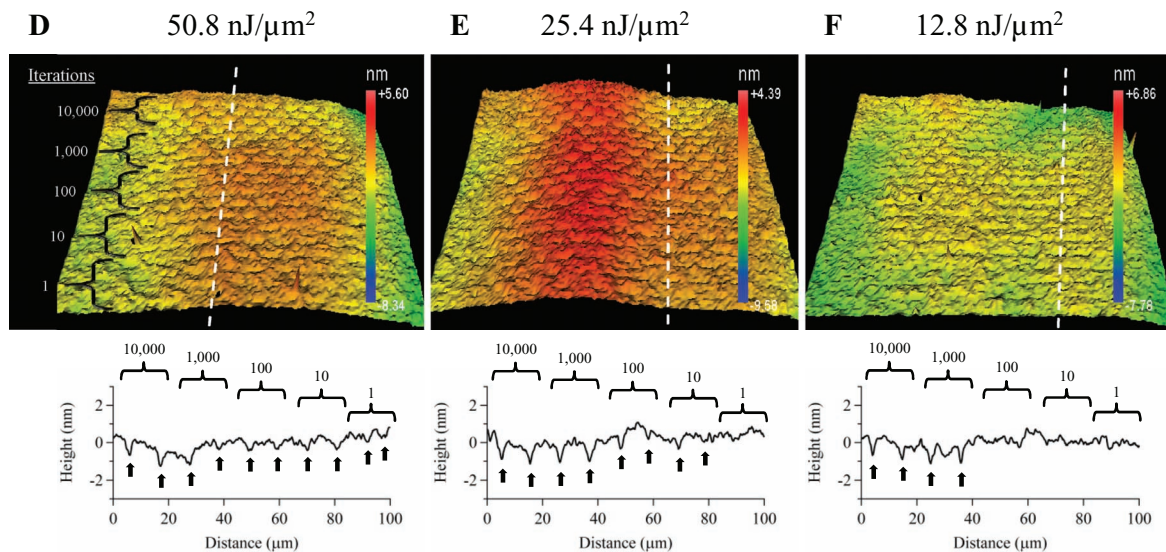


Figure 5. Patterning with Controlled Topography. 6 and 10 nm thick Au films were functionalized with an OEG-terminated alkanethiol and arrays of 1×20 pixel ROIs of the OEG SAM were thermally desorbed with a 532 nm laser focused through a $20\times$ (NA0.8) objective with varying laser fluence ($50.8\text{--}12.8 \text{ nJ } \mu\text{m}^{-2}$) and number of iterations (10 000–1) per ROI. Surface topography maps of patterned (A–C) 6 nm and (D–F) 10 nm Au films were created with white light interferometry. Height traces of the surface topography were acquired as depicted by the dashed white lines. Raised topographical patterning occurred only on 6 nm thick Au films (≥ 10 iterations at (A) 50.8 or (B) 25.4 $\text{nJ } \mu\text{m}^{-2}$ and ≥ 100 iterations at (C) 12.8 $\text{nJ } \mu\text{m}^{-2}$) and the extent of the topography increased with increased fluence and number of iterations from nearly flat at low laser energy and/or low number of iterations to ~ 17 nm at high laser energy and/or increased iterations. (D–F) The higher thermal conductivity of the 10 nm Au films prevented hydrodynamic melting of the Au and only vaporization or chemically-specific patterning occurred. Vaporization of the Au in the patterned regions on 10 nm films resulted in 0.5–1.0 nm indentations (black arrows in the height traces as indicated in (D–F)). The pattern depth decreased with decreased laser energy and/or fewer iterations. The data demonstrates that LSL allows fabrication of micropatterns with controlled topography on the nanometer length scale.

to gain insight into the relationships between the light intensity profile, surface temperature profile, and extent of SAM desorption.^[35] In their setup, the surface area that exceeded a

temperature of 212 °C was always larger than the laser beam waist.^[35] Since the temperature profile in the Au film follows a Gaussian distribution where size is determined by the Airy

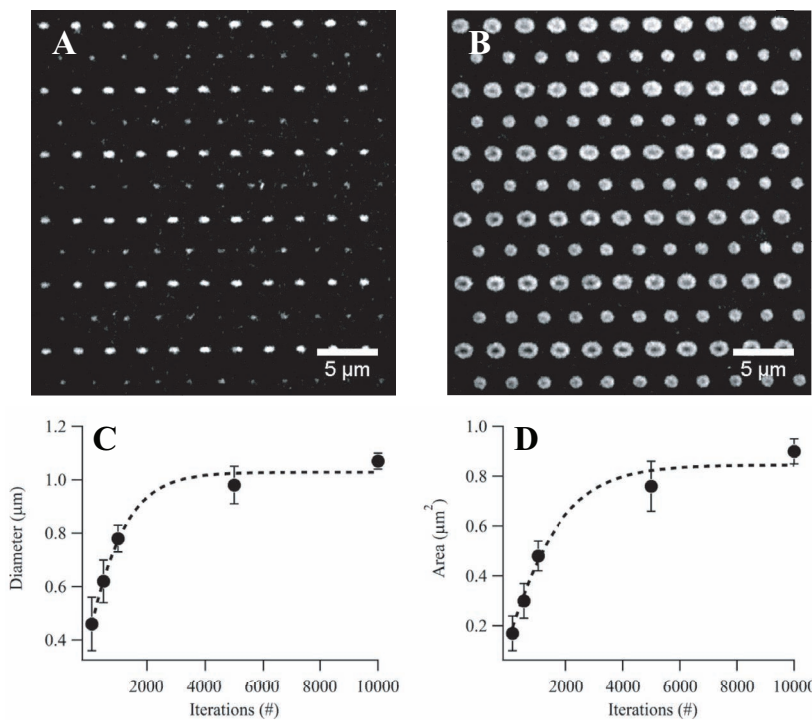


Figure 6. Nanopattern Fabrication with LSL. 10 nm Au films were functionalized with an OEG-terminated alkanethiol and a mixed array of 1 × 1 and 1 × 3 pixel ROIs was used to thermally desorb the OEG SAM with a 532 nm laser focused through a 6× (NA 1.4) oil immersion objective ($33.38 \text{ nJ } \mu\text{m}^{-2}$) with iterations varying from 125 –10 000 per ROI. The surfaces were exposed to HFN, the HFN labeled, and the surfaces imaged. Fluorescently labeled HFN adsorbed to the patterned array created with A) 125 iterations or B) 10 000 iterations per ROI. The C) diameter and D) area of the circular patterns increased with increased iterations due to spreading of the heat through the Au films. A,C) Patterns as small as 460 nm ($0.17 \mu\text{m}^2$) were created using LSL. SB = 5 μm.

Disk, laser intensity, scan speed, and thermal conductivity of the film, it should be possible to use low fluence in combination with low conducting films to create patterns with only the tip of the Gaussian profile. This mode of patterning could provide the ability to confine the surface area that reaches the threshold for SAM desorption to be smaller than the Airy Disk. Minimization of the energy delivered to the Au film combined with the use of low conductivity films allowed the fabrication of sub-diffraction limited patterns. A 532 nm laser focused through a 20× (NA 0.8) objective operating at a fluence of $7.55 \text{ nJ } \mu\text{m}^{-2}$ was used to pattern 6 nm Au films. Elliptical patterns with an average minor axis of $594 \pm 154 \text{ nm}$, which is 26% smaller than the 811 nm Airy Disk, were created. While this is the first report, to our knowledge, of sub-diffraction limited thermal patterning of SAMs on Au surfaces, sub-diffraction limited patterning with laser-assisted desorption of silane and siloxane SAMs on oxidized silicon surfaces has been demonstrated.^[46–50] Silane and siloxane SAMs inherently have a higher activation energy for thermal desorption due to their ability to bind not only to the surface, as with alkanethiol SAMs, but to also crosslink with neighboring molecules.^[49,51] Due to this higher activation energy, the ability to create sub-diffraction limited patterns up to 97% smaller than the laser beam waist has been reported.^[46,47,49]

2.4. Patterned Arrays That Present Ligand Concentration Gradients

Surfaces presenting ligand concentration gradients are useful for investigating fundamental cell processes such as polarization^[52] and migration.^[53] We implemented two complementary patterning methods that relied on dose dependent changes in the total energy delivered to the Au film to create either stepwise or smooth surface concentration gradients of alkanethiol SAMs (Figure 7). 10 nm thick Au films were functionalized with an OEG-terminated alkanethiol. The OEG SAM was thermally desorbed using two methods to vary the amount of energy delivered to the patterned regions by either changing the number of iterations used in adjacent patterns (Figure 7A) or by slightly tilting the sample (Figure 7B). The patterned surfaces were functionalized with a biotin-terminated alkanethiol followed by exposure to AF546-conjugated streptavidin. The first method was implemented to create a symmetrical gradient displaying stepwise changes in the ligand concentration between each column (Figure 7C–E). The number of iterations used to pattern the ROIs in adjacent columns was decreased by a factor of 2 from the left column to center and increased by a factor of 2 from the center column to the right (Figure 7C). This method resulted in stepwise changes in fluorescent intensity between adjacent columns (Figure 7C–E). Alternatively, the amount of energy delivered

to the films can be decreased more smoothly by slightly tilting the sample so that the focal plane of the laser slowly retracts from the surface.^[29] The last column on the right (Figure 7C) was patterned by tilting the sample 1.4° so that the sample slowly left the focal plane of the objective from the top row to the bottom row (~2 μm out of focus over 80 μm) resulting in a smoother ligand concentration gradient (Figure 7C,D).

2.5. Ligand Surface Density Displayed by HFN and Mixed SAMs of GRGD- and OEG-Terminated Alkanethiols

Since ligand density influences cell adhesion, spreading, and motility,^[54–56] it is crucial to know the densities of the ligands displayed by the multifaceted surfaces in order to perform detailed cell studies. XPS was implemented to estimate the RGD ligand surface density displayed by HFN adsorbed to bare Au and by surfaces functionalized with mixed GRGD/OEG alkanethiol SAMs.

2.5.1. Estimation of RGD Surface Density Displayed by HFN Adsorbed to Au

High-resolution C_{1s}, N_{1s}, and Au_{4f} XPS spectra were attained for Au surfaces exposed to HFN solution (30 min at 37 °C) at

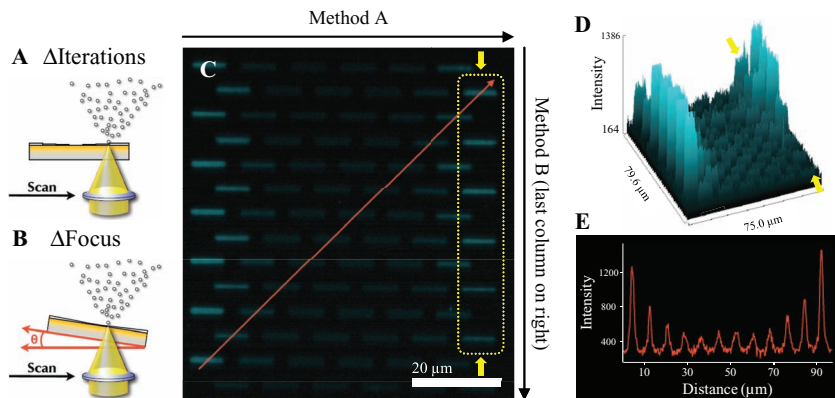


Figure 7. Fabrication of Micrometer-Scale Ligand Gradients. LSL provides two methods to create ligand density gradients. The total amount of energy delivered to the ROIs can be varied by changing the number of iterations per ROI as depicted in (A) or by slightly tilting the sample so that the sample slowly leaves the focal plane of the laser as depicted in (B). C) A 10 nm Au film was functionalized with an OEG-terminated alkanethiol and $1 \mu\text{m} \times 8 \mu\text{m}$ patterns of the OEG were thermally desorbed with a 532 nm laser. The bare Au patterns were backfilled with a biotin-terminated alkanethiol, labeled with AF546-conjugated streptavidin, and imaged. The number of iterations per ROI was decreased by a factor of 2 from the left to the center of the image and increased by a factor of 2 from the center to the right of the image to create a symmetrical density gradient using the method depicted in (A). C) The last column on the right (outlined by dashed yellow line and indicated by the yellow arrows) was created by tilting the sample 1.4° so that the laser slowly went out of focus from the top to bottom using the method depicted in (B). D) An areal plot of the streptavidin fluorescent intensity shows the gradients created in the x direction across all columns and in the y direction for the last column on the far right in (C) as indicated by the yellow arrows. E) A line plot of the streptavidin intensity as indicated by the red line in (C). (B) SB = 20 μm .

concentrations of $1.56\text{--}50.00 \mu\text{g mL}^{-1}$ to monitor the adsorption of HFN and to create an RGD surface density calibration graph (Figure S1, Figure 8A). Deconvolution of the C_{1s} spectra indicated the presence of C-C (285 eV: ~43%), amine, alcohol, ether (286 eV: ~34%), and amide (288 eV: ~23%) bonds on the surface (Figure S1, Table S1). Incremental increases in the C_{1s} and N_{1s} signal intensities accompanied by a decrease in the Au_{4f} background signal were observed as the HFN solution concentration increased, affirming increased HFN adsorption with increased solution concentration (Figure S1, Table S1). The packing density of a monolayer of fibronectin is $\sim 190 \text{ ng cm}^{-2}$ ($\sim 2500 \text{ FN } \mu\text{m}^{-2}$) as determined through radiolabeling experiments.^[57] The measured area under the N_{1s} peak for the surfaces exposed to HFN solution at $50 \mu\text{g mL}^{-1}$ was set to the saturation value of $2500 \text{ FN } \mu\text{m}^{-2}$. The HFN packing density for the surfaces exposed to lower HFN concentrations was determined using the relative areas under the N_{1s} peaks to ratiometrically back calculate the packing density.^[45] As a metric for comparison between the HFN and GRGD SAMs, the number of RGD motifs per area was calculated. The RGD density displayed by adsorbed HFN was estimated by multiplying the HFN packing density by 2 (the number of RGD motifs per HFN molecule). Using this method, an RGD surface density calibration graph was created (Figure 8A). A sigmoidal relationship between the number of RGD motifs displayed and the solution concentration of HFN was observed. The RGD density linearly increased from 963 ± 258 to $4,106 \pm 203 \text{ RGD } \mu\text{m}^{-2}$ at HFN solution concentrations of 1.56 and $12.50 \mu\text{g mL}^{-1}$ respectively that reached a saturation value of $5,000 \pm 131 \text{ RGD } \mu\text{m}^{-2}$ at $50.00 \mu\text{g mL}^{-1}$. Although this measure does not take other

integrin binding domains displayed by HFN into account, it provides a metric for comparing to the GRGD SAM patterns.

2.5.2. Estimation of GRGD Surface Density Displayed by Mixed SAMs of GRGD- and OEG-terminated Alkanethiols

The GRGD ligand density displayed by mixed SAMs of GRGD- and OEG₃-terminated alkanethiols was estimated with the same method used to determine the HFN packing density. Surfaces displaying mixed SAMs of GRGD/OEG₃ were created by varying the molar ratio of the two alkanethiols at a constant working concentration of 2 mM. For example, a 10% GRGD surface was created by functionalizing the Au with a solution containing equal volumes of 0.2 mM GRGD and 1.8 mM OEG₃. Surfaces presenting mixed SAMs of GRGD/OEG₃ composed of $\leq 1\%$ GRGD prevent adsorption of protein from solution^[4] and at 1% GRGD display an RGD packing density of $\sim 7.5 \text{ pmol cm}^{-2}$ ($45\text{--}165 \text{ RGD } \mu\text{m}^{-2}$).^[58] To estimate the GRGD packing density, surfaces were functionalized with mixed GRGD/OEG₃ SAMs with the %GRGD varied from 0–10%. High resolution C_{1s} , N_{1s} , O_{1s} , and Au_{4f}

XPS spectra were acquired for each surface (Figure S2). Incremental increases in the N_{1s} signal intensity accompanied by increases in both the OEG (287 eV) and amide bond (288 eV) portions of the C_{1s} spectra were observed with

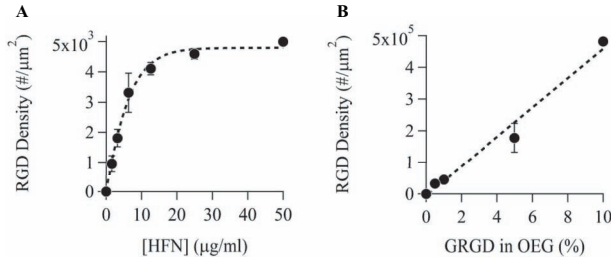


Figure 8. RGD Surface Density Displayed by Adsorbed HFN and Mixed GRGD/OEG₃ SAMs. XPS was used to estimate the RGD surface density displayed by HFN adsorbed to bare Au or by mixed GRGD/OEG₃ alkanethiol SAMs. (A) Bare Au surfaces were exposed to HFN solution with concentrations from $1.5\text{--}50.0 \mu\text{g mL}^{-1}$ and the N_{1s} spectra acquired with XPS at each concentration (see Supplemental Figure S1 and Table S1). The area under the N_{1s} peak was measured for each condition to quantify the amount of protein present, and the HFN surface density was ratiometrically back calculated. The RGD surface density was determined by multiplying the HFN density by the number of RGD motifs, two, displayed on each HFN molecule. B) A similar method was used to estimate the RGD surface density displayed by mixed SAMs of GRGD- and OEG₃-terminated alkanethiols. Bare Au surfaces were exposed to solutions of mixed alkanethiols at a working concentration of 2 mM for 1 h. The percent of GRGD-terminated alkanethiol in solution was varied from 0.5–10.0%. The area under the N_{1s} peak (see Supplemental Figure S2 and Table S2) was used to ratiometrically back calculate RGD surface density.

increasing %GRGD affirming an increased surface density of GRGD in the mixed SAM (Figure S2, Table S2). Concurrently, a decrease in the Au_{4f} background signal with increased %GRGD was observed due to increased shadowing from the longer GRGD alkanethiol (Figure S2, Table S2). The GRGD packing density of the surfaces created with 1% GRGD was set to 45 165 RGD μm^{-2} ^[58] and the packing densities of the remaining surfaces were ratiometrically back calculated using the relative areas under the N_{1s} peaks. The GRGD packing density linearly increased from 32 809 \pm 7,704 to 481 813 \pm 5274 RGD μm^{-2} as the %GRGD increased from 0.5 to 10.0% respectively (Figure 8B).

2.6. Cell Adhesion & Migration on Multifaceted Patterned Surfaces

2.6.1. Simultaneous Cell Adhesion to Multiple Patterned Ligands on Multifaceted Surfaces

To confirm bioactivity of the patterned ligands and to examine adhesion site placement, human umbilical vein endothelial cells (HUVECs) were cultured on multifaceted, micropatterned surfaces that displayed an array of 1 $\mu\text{m} \times$ 8 μm ellipses of GRGD (1% GRGD in OEG₆: 45 165 RGD μm^{-2}) in the horizontal direction orthogonally interwoven with an array of 1 $\mu\text{m} \times$ 8 μm ellipses of HFN (25 $\mu\text{g mL}^{-1}$: 4 593 RGD μm^{-2}) in the vertical direction (Figure 9). It should be noted that mixed SAMs of GRGD in OEG₆ were used for cell studies instead of the GRGD/OEG₃ SAMs used for XPS analysis. OEG₆ displays increased resistance to protein adsorption compared to OEG₃^[59–61] and it was crucial to prevent HFN adsorption to the GRGD patterns during the fabrication of the multifaceted surfaces. It should also be noted that mixed SAMs of GRGD in either OEG₃ or OEG₆ display a similar RGD packing density therefore the RGD density displayed by the GRGD/OEG₃ SAMs determined through XPS analysis also reflects the RGD density for the GRGD/OEG₆ SAMs.^[58] 16 h post seeding the HUVECs were fixed, fluorescently immunolabeled for HFN, vinculin, and actin, and imaged. Fluorescent labeling of HFN was used to confirm preferential adsorption of HFN to the bare Au patterns (see insets 1 & 2 in Figure 9). HUVECs cultured on multifaceted, patterned surfaces formed adhesions simultaneously to both the GRGD (red arrows) and HFN (blue arrows) patterns as indicated by vinculin labeling (Figure 9). These results indicate that both ligands retained bioactivity during the LSL patterning process and that HUVECs recognized and adhered to both GRGD and HFN patterns. To our knowledge, this is the first demonstration of simultaneous cell adhesion to multiple patterned ECM ligands in a single cell.

2.6.2. Lamella Formation and Migration on Multifaceted Patterned Surfaces

After demonstrating bioactivity and simultaneous cell attachment to both patterned ligands, we implemented multifaceted surfaces to monitor how HUVECs utilized the two different ligands during migration. HUVECs were seeded on the same surfaces described in Section 2.6.1 and imaged with time-lapse

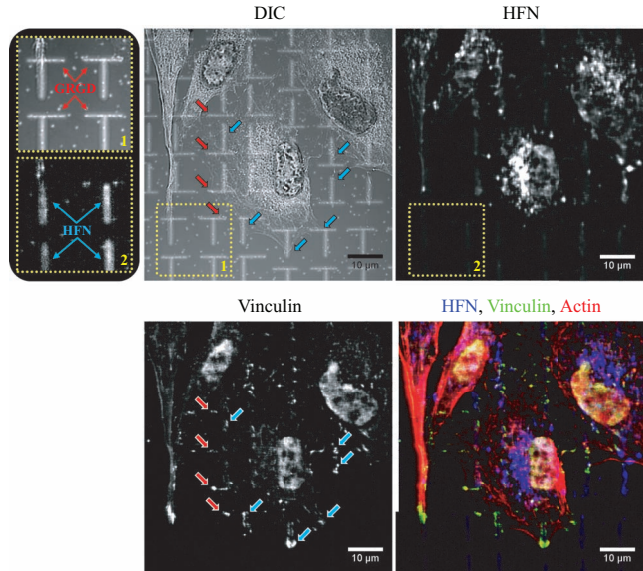


Figure 9. HUVEC Adhesion Site Formation on Multifaceted Patterned Surfaces. Multifaceted patterned surfaces presenting 1 $\mu\text{m} \times$ 8 μm ellipses of GRGD-terminated alkanethiol in the horizontal direction (1% GRGD in OEG: see inset 1) interwoven with HFN ellipses in the vertical direction (25 $\mu\text{g mL}^{-1}$: see insets 1 and 2) were prepared with LSL. The GRGD and HFN patterns displayed an RGD surface density of \sim 45 165 and 4593 RGD μm^{-2} , respectively (see Figure 8). To determine the placement of the HUVEC adhesion sites and which ligand was being ligated, the HUVECs were fixed 16 h post seeding, immunolabeled for HFN (top right), vinculin (bottom left), and actin (red in bottom right), and imaged with fluorescent and differential interference contrast (DIC) (top left) microscopies. HUVECs displayed adhesions to both the GRGD (red arrows) and HFN (blue arrows) patterns. The data demonstrates that both ligands were biologically active after patterning and induced integrin ligation and adhesion site formation. SB = 10 μm .

differential interference contrast (TL-DIC) microscopy 6 h post seeding. Figure 10 displays a time series of DIC images for a representative HUVEC migrating on a multifaceted surface. At t = 0 min (equivalent to 6 h post seeding) most HUVECs displayed alignment and elongation to the long axis of the vertical HFN patterns. As time proceeded, cells used both GRGD and HFN patterns during lamella formation while maintaining preferential elongation to HFN ellipses. At t = 4 min, a membrane extension guided along a GRGD pattern was formed. Over the next 4 minutes the extension extended vertically downward guided along a HFN pattern and terminated on a GRGD pattern. The lamella continued to grow vertically guided by the HFN patterns and eventually covered three additional HFN patterns and terminated on GRGD patterns at the top and bottom. Interestingly, the HFN patterns dominated the direction of cell elongation even when the RGD density was an order of magnitude lower than displayed by the GRGD patterns. While not fully understood, we speculate that additional binding domains available in HFN could influence adhesion site positioning through either differential integrin usage or adhesion site kinetics or that the process of fibrillogenesis could play a role in the orientation of the HUVECs to the long axis of the HFN patterns.

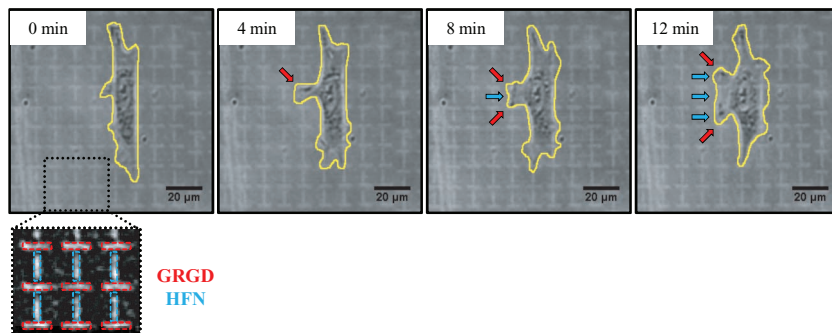


Figure 10. HUVECs Utilize both GRGD & HFN Patterns During Lamella Formation & Migration on Multifaceted Surfaces. Multifaceted patterned surfaces presenting $1\text{ }\mu\text{m} \times 8\text{ }\mu\text{m}$ ellipses of GRGD-terminated alkanethiol (1% in OEG: horizontal patterns outlined in red in inset) interwoven with HFN ellipses ($25\text{ }\mu\text{g mL}^{-1}$: vertical patterns outlined in blue in inset) were prepared with LSL. The GRGD and HFN patterns displayed an RGD surface density of $\sim 45\text{ }165$ and $4593\text{ }\mu\text{m}^{-2}$ respectively (see Figure 8). HUVECs were seeded on the surfaces and imaged with TL-DIC microscopy 6 h post seeding. HUVECs on multifaceted surfaces displayed preferential cell elongation parallel to the long axis of the HFN patterns and used both GRGD and HFN patterns during lamella formation as shown by a representative HUVEC outlined in yellow. ($t = 0\text{ min}$) The HUVEC was initially elongated in a direction parallel to the long axis of the HFN patterns. ($t = 4\text{ min}$) Over the next four min, the HUVEC produced a membrane extension along one of the GRGD patterns as depicted by the red arrow. ($t = 8\text{ min}$) A lamella began to form that spanned an additional HFN pattern (blue arrow) and terminated at another GRGD pattern (bottom red arrow). ($t = 12\text{ min}$) Vertical growth of the lamella occurred along the HFN patterns and spanned three additional HFN patterns (blue arrows) and displayed termini on two GRGD patterns (red arrows). The use of GRGD patterns to span to neighboring HFN patterns was observed in HUVECs migrating on multifaceted surfaces. SB = $20\text{ }\mu\text{m}$.

3. Conclusions

While a multitude of surface patterning strategies exists, there are very few “maskless” techniques and even fewer techniques that allow the fabrication of multifaceted patterned surfaces that display multiple ligands with each ligand confined to its own patterned array. We demonstrated that LSL is a highly versatile “maskless” surface patterning strategy that allows the fabrication of surfaces that i) display nano- to micrometer-sized patterns of adhesive ligand, ii) have well-controlled pattern topography on the nanometer length scale, and iii) display both stepwise and smooth ligand gradients. More importantly, LSL provides the ability to pattern multiple adhesive ligands in close proximity. We created multifaceted patterned surfaces displaying interwoven arrays of GRGD and HFN with each ligand confined to its own array. HUVECs cultured on these surfaces formed vinculin-containing adhesions simultaneously to both ligands. While GRGD and HFN were used as model ligands in this study, the ability to pattern multiple peptides or proteins could be easily achieved.

The flexibility in pattern properties with respect to size, spacing, geometry, topography, and ligand density provides the ability to simultaneously investigate a number of influences of ligand display on cell adhesion and behavior. For example, nanoscale surface topography can enhance certain aspects of cell behavior (proliferation,^[62,63] adhesion,^[62] mineralization^[63]) in osteoblasts and disrupt some processes (adhesion, cytoskeletal formation) in fibroblasts.^[64] While the underlying mechanisms of nanotopography-induced changes in cell behavior remain elusive, Miller et al. proposed that the observed cellular

changes may simply be caused by differences in protein surface concentration or conformation.^[65] Using LSL, patterns with systematic variations in both topography and ligand concentration could be fabricated in close proximity with high spatial resolution allowing the fabrication of surfaces displaying varying levels of nanotopography on a single surface. Experiments with such surfaces could allow detailed studies of the influences of nano-scale topography and ligand concentration to be conducted simultaneously and even in a single cell, if desired.

4. Experimental Section

Materials: 25 and 35 mm diameter, # 1, optical borosilicate circular glass coverslips, sulfuric acid (H_2SO_4), 30% hydrogen peroxide (H_2O_2), and sodium chloride (NaCl) were purchased from Fisher Scientific (Pittsburgh, PA). Millipore water (MPH_2O) with a resistance $>18\text{ M}\Omega\text{-cm}$ was obtained from a Millipore Super-Q water system (Billerica, MA). $1/8'' \times 1/8''$, 99.999% pure Titanium and gold pellets and 7cc molybdenum crucibles were purchased from Kamis Inc. (Mahopac Falls, NY). 30% ammonium hydroxide (NH_4OH), 200 proof ethanol, and T-25 tissue culture flasks were purchased from VWR (West Chester, PA). Ultrahigh purity nitrogen (N_2) was purchased from Matheson TriGas (Basking Ridge, NJ).

$\text{HS}(\text{CH}_2)_{15}\text{CONHCH}_2\text{CH}_2(\text{OCH}_2\text{CH}_2)_5\text{OH}$ (OEG) and $\text{HS}(\text{CH}_2)_{15}\text{CONHCH}_2\text{CH}_2(\text{OCH}_2\text{CH}_2)_{11}\text{GRGDS}$ (GRGDS) alkanethiols were synthesized as previously reported.^[66] $\text{HS}(\text{CH}_2)_{11}(\text{OCH}_2\text{CH}_2)_3\text{OH}$ (OEG_3), $\text{HS}(\text{CH}_2)_{11}(\text{OCH}_2\text{CH}_2)_6\text{OH}$ (OEG₆), and $\text{HS}(\text{CH}_2)_{11}(\text{OCH}_2\text{CH}_2)_6\text{GRGD}$ (GRGD) alkanethiols were purchased from ProChimia (Sopot, Poland). Human plasma fibronectin (HFN), heat-shocked bovine serum albumin (BSA), Tween20, TritonX-100, sucrose, 4-(2-hydroxyethyl)-1-piperazineethanesulfonic acid (HEPES), magnesium chloride (MgCl_2), monoclonal mouse anti-vinculin, anhydrous N,N-dimethylformamide (DMF), and triethylamine (Et_3N) were purchased from Sigma-Aldrich (St. Louis, MO). Phosphate buffered saline (PBS), pooled human umbilical vein endothelial cells (HUVECs), endothelial cell growth medium-2 (EGM-2), EGM-2 SingleQuots kits, and 0.25% trypsin with 1 mM ethylenediaminetetraacetic acid (EDTA) were purchased from Lonza (Basel, Switzerland). Alexa Fluor 633 (AF633) carboxylic acid succinimidyl ester, AF405, AF488, and AF532 protein labeling kits, goat serum, AF405 goat anti-rabbit, AF532 phalloidin, AF488 goat anti-mouse, and Prolong Antifade Gold were purchased from Invitrogen (Carlsbad, CA). Rabbit anti-HFN was purchased from Abcam (Cambridge, MA). EM grade 16% paraformaldehyde in de-ionized H_2O was purchased from Electron Microscopy Sciences (Hatfield, PA).

Synthesis of ω -Functionalized Alkanethiols: OEG-, GRGDS-, and biotin-terminated alkanethiols were synthesized as previously described.^[66] GRGDS- and biotin-terminated alkanethiols were more efficiently synthesized through the use of NovaSyn™ TGA resin (EMD Chemicals Inc., Gibbstown, NJ), which is composed of a 4-hydroxy-methyl-phenoxy-acetic acid linker attached to a PEG spacer coupled to the polystyrene resin. To improve yield of each step, we also employed double couplings of each amino acid with each coupling at a 5× molar excess. Coupling of the trityl-protected alkanethiol to the peptide-resin was allowed to proceed for 12 h for each coupling at a 5× molar excess. Reversed-phase high performance liquid chromatography was performed with a preparative-scale 21.5 mm C18 column using a gradient of 95% A) 45:55 isopropanol:water + 0.05% TFA to 95% B) isopropanol + 0.05% TFA over

40 min at 5 mL min⁻¹ flow rate (higher flow rates could not be utilized due to the tendency of pumped isopropanol to spontaneously form air bubbles). ω -Functionalized alkanethiols were purified to $\geq 95\%$ purity and verified for identity by matrix assisted laser desorption ionization time of flight mass spectrometry (MALDI-ToF; Bruker Daltonics, Billerica, MA).

Metal Deposition: Coverslips were cleaned in piranha solution (3:1 H₂SO₄:H₂O₂) for 1 h, rinsed thoroughly in MPH₂O, soaked in MPH₂O overnight, and dried with N₂. For LSL patterning, 2 nm Ti and 6, 8, or 10 nm Au were deposited at a rate of 1–2 Å sec⁻¹ onto 35 mm diameter coverslips and for XPS studies 10 nm Ti and 75 nm Au were deposited onto 25 mm coverslips using an electron-beam evaporator (Sharon Vacuum, Brockton, MA). The film thickness and deposition rate were monitored by the quartz crystal located adjacent to the sample stage in the evaporator.

Laser Characterization: The diameter of the focused laser beam was estimated from the Airy Disk as shown in Equation 1:

$$AD = \frac{1.22\lambda}{NA} \quad (1)$$

where AD is the Airy Disk diameter (beam waist of the focused laser), λ the wavelength, and NA the numerical aperture of the objective. The power output (P) of the laser was measured at the focal plane of the objective and the intensity (I) was calculated from Equation 2:

$$I = \frac{P}{AD} = \frac{P \times NA}{1.22\lambda} \quad (2)$$

The energy input into each pixel of the ROI was tuned by changing the pixel dwell time (D_t); the time that the laser resides at each pixel in the ROI during patterning. Operating at the same intensity with varied (D_t) allowed control over the laser fluence (F) as described by Equation 3:

$$F = I \times D_t = \frac{P \times NA \times D_t}{1.22\lambda} \quad (3)$$

Supplementary Tables 3 and 4 provide a comprehensive list of the measured and calculated laser parameters described in Equation 1–3 for the 20 \times (NA0.8) and 63 \times (NA1.4) objectives respectively.

Surface Fabrication and Pattern Characterization: Metalized coverslips were cleaned in dilute TL1 (6:1:1 MPH₂O:NH₄OH:H₂O₂) at 80 °C for 1–2 min, rinsed with MPH₂O, dried with N₂, and immediately functionalized with a 2 mM ethanolic solution of OEG₆ overnight, rinsed with ethanol, and dried with N₂. Desired ROIs of the OEG SAM were thermally desorbed using the “Edit Bleach” software on a Zeiss 5Live laser scanning confocal microscope (Carl Zeiss, Munich, Germany) equipped with an automated stage. ROIs were exposed to a 532 nm laser focused through a 20 \times (NA 0.8) air or 63 \times (NA 1.4) oil immersion objective. Patterning with a 532 nm laser operating at 12.8 nJ µm⁻² using 1 000 iterations per ROI allowed the fabrication of 1 mm × 1 mm arrays in ~45 min. Patterning was performed in a 37 °C, N₂-rich environment to facilitate thiol desorption from the surface. For single ligand pattern characterization studies, the first set of ROIs were functionalized with either a 2 mM ethanolic solution of 1% GRGDS in OEG₆ or with AF405-conjugated HFN at 12.5 µg mL⁻¹ in PBS. For multifaceted surface characterization, the first set of ROIs was functionalized with a 2 mM ethanolic solution of GRGDS and the GRGDS fluorescently labeled with a 1:100 dilution of AF633 carboxylic acid succinimidyl ester in DMF with 100 mM Et₃N for 10 h. The surfaces were rinsed with DMF, rinsed with ethanol, and dried with N₂. The surfaces were patterned again with a second set of ROIs, exposed to 500 µL of AF405-conjugated HFN at a concentration of 10–25 µg mL⁻¹ in PBS for 30 min at 37 °C, rinsed with PBS, rinsed with MPH₂O, and dried with N₂. The samples were imaged on a Zeiss 5Live confocal microscope (Carl Zeiss, Munich, Germany) with a 20 \times (NA0.8) air objective using 405 nm excitation and a LP420 emission filter for the AF405-conjugated HFN and with 635 nm excitation and a LP650 emission filter for the AF633 labeled GRGDS. Images of the

HFN patterns were thresholded and each pattern was mathematically fit with an ellipse to determine the area, minor axis, and major axis using ImageJ (NIH, Bethesda, MD). To investigate the influence of the laser properties on feature size, the elliptical patterns were created with systematic variations in laser power, intensity, fluence, and the number of iterations per ROI. To determine the influence of Au surface thickness (thermal conductivity) on pattern feature size, the same experiments were performed on 6, 8, and 10 nm Au samples. The same patterning procedure was implemented to create surfaces for cell studies with the following exceptions: i) a mixed SAM of 1% GRGD in OEG₆ was used to create the GRGD patterns instead of 2 mM GRGDS and ii) fluorescent pre-labeling of the GRGD and HFN were excluded.

XPS Measurements: C_{1s}, N_{1s}, O_{1s}, and Au_{4f} spectra were obtained at a 45° takeoff angle using a PHI Quantera XPS scanning microprobe (Physical Electronics, Chanhassen, MN) equipped with a 114.8 W monochromatic aluminum X-ray source. High resolution scans were acquired with a 200 µm spot size, a pass energy of 26 eV, and a step size of 0.1 eV. All spectra were referenced to the Au_{4f} peak at 84 eV. The high resolution spectra were deconvolved with Gaussian fits using PeakFit software (Systat Inc., Chicago, IL) to analyze the bond types present and to measure the area under each spectrum. Surface mapping XPS images were obtained using a 9 µm spot size and a pass energy of 140 eV with a step size of 15 eV.

Interferometry Measurements: Surface topography maps were acquired with a Zygo NewView 6200 (Zygo Inc., Middlefield, CT) white light interferometer. Surface topography images were acquired with a 50 \times objective and a z-scan of ± 20 µm. Five scans were averaged per viewfield and the resulting image flattened with a plane-fit compensation filter.

Cell Culture: HUVECs were cultured at 37 °C and 5% CO₂ in EGM-2 basal media supplemented with 10 mL fetal bovine serum, 0.2 mL hydrocortisone, 2 mL hFGF-B, 0.5 mL VEGF, 0.5 mL R3-IGF-1, 0.5 mL ascorbic acid, 0.5 mL hEGF, 0.5 mL gentamicin-amphotericin-B, and 0.5 mL heparin in a HFN coated (3 mL at 12.5 µg mL⁻¹ for 30 min at 37 °C) T-25 tissue culture flask. When 80% confluence was reached, the cells were trypsinized with 3 mL of 0.25% trypsin and 1 mM ethylenediaminetetraacetic acid in PBS at 37 °C for 3 min. The cells were collected and centrifuged for 10 min. The cell pellet was re-suspended in full EGM-2 media and seeded on patterned surfaces at a density of ~ 15 cells mm⁻². Passage 3 HUVECs were used for all experiments.

Time-lapse DIC Microscopy & Fluorescent Immunolabeling & Imaging: After 6 h in culture, HUVECs on multifaceted patterned surfaces were imaged with time-lapse differential interference contrast microscopy using the “time series” application on a Zeiss 5Live confocal microscope (Carl Zeiss, Munich, Germany). A 532 nm laser focused through a 20 \times (NA 0.8) objective operating at the lowest power setting was used for excitation and images were acquired at 2 min intervals for 2 h.

After 16 h in culture, the HUVECs were fixed and labeled for HFN, actin, and vinculin. The surfaces were gently rinsed with warm PBS-T (PBS supplemented with 0.01% Tween 20), submerged into an ice-cold cytoskeleton stabilizing buffer (0.5% Triton X-100, 300 mM sucrose, 10 mM HEPES, 3 mM MgCl₂, 50 mM NaCl in MPH₂O, pH 6.8) for 1 min, submerged into ice-cold 4% paraformaldehyde in PBS-T, and placed in a 37 °C water bath for 10 min. The samples were removed from the paraformaldehyde, rinsed with PBS-T, blocked with 10% goat serum in PBS-T for 1 h, rinsed with PBS-T, and incubated with 500 µL of primary antibody solution (1 µg mL⁻¹ rabbit anti-HFN, 5 µg mL⁻¹ mouse anti-vinculin, 1:20 dilution AF532 phalloidin in PBS-T) O/N at 4 °C. The samples were rinsed with PBS-T, incubated with 1 mL of secondary antibody solution (10 µg mL⁻¹ AF488 goat anti-mouse and 10 µg mL⁻¹ AF405 goat anti-rabbit in PBS-T) for 1 h, rinsed with PBS-T, rinsed with MPH₂O, and gently dried with N₂. A drop of Prolong Antifade Gold was added to the surface and secured with a coverslip. The samples were imaged on a Zeiss 5Live confocal microscope. The AF405 labeled HFN was imaged with 405 nm excitation and a BP415–480 emission filter, the AF488 labeled vinculin with 488 nm excitation and a BP500–525 emission filter, and the AF532 labeled actin with 532 nm excitation and a LP550 emission filter. The brightness, contrast, and color balance were adjusted and merged images were created using ImageJ (NIH, Bethesda, MD).

Supporting Information

Supporting Information is available from the Wiley Online Library or from the author.

Acknowledgements

We thank Tomasz Tkaczyk and Robert Kester for assistance with interferometry. This work was supported by grants from the National Institutes of Health (HL097520), and a NIH F31 Training Grant (J.S.M., EB005558). J.H.S. was supported by postdoctoral fellowships from the NIH Nanobiology Training Program of the Keck Center of the Gulf Coast Consortia and from HHMI.

Received: February 7, 2011

Revised: April 12, 2011

Published online: May 31, 2011

- [1] N. Sniadecki, R. A. Desai, S. A. Ruiz, C. S. Chen, *Ann. Biomed. Eng.* **2006**, *34*, 59.
- [2] W. Senaratne, L. Andruzzi, C. K. Ober, *Biomacromolecules* **2005**, *6*, 2427.
- [3] R. Levicky, T. M. Herne, M. J. Tarlov, S. K. Satija, *J. Am. Chem. Soc.* **1998**, *120*, 9787.
- [4] C. Roberts, C. S. Chen, M. Mrksich, V. Martichonok, D. E. Ingber, G. M. Whitesides, *J. Am. Chem. Soc.* **1998**, *120*, 6548.
- [5] E. Ostuni, L. Yan, G. M. Whitesides, *Colloids Surf. B* **1999**, *15*, 3.
- [6] B. T. Houseman, E. S. Gawalt, M. Mrksich, *Langmuir* **2003**, *19*, 1522.
- [7] R. Singhvi, A. Kumar, G. P. Lopez, G. N. Stephanopoulos, D. I. C. Wang, G. M. Whitesides, D. E. Ingber, *Science* **1994**, *264*, 696.
- [8] R. McBeath, D. M. Pirone, C. M. Nelson, K. Bhadriraju, C. S. Chen, *Dev. Cell* **2004**, *6*, 483.
- [9] K. A. Kilian, B. Bugarija, B. T. Lahn, M. Mrksich, *Proc. Natl. Acad. Sci. USA* **2010**, *107*, 4872.
- [10] A. D. Doyle, F. W. Wang, K. Matsumoto, K. M. Yamada, *J. Cell Biol.* **2009**, *184*, 481.
- [11] N. Xia, C. K. Thodeti, T. P. Hunt, Q. B. Xu, M. Ho, G. M. Whitesides, R. Westervelt, D. E. Ingber, *FASEB J.* **2008**, *22*, 1649.
- [12] A. Brock, E. Chang, C. C. Ho, P. LeDuc, X. Y. Jiang, G. M. Whitesides, D. E. Ingber, *Langmuir* **2003**, *19*, 1611.
- [13] M. Thery, V. Racine, M. Piel, A. Pepin, A. Dimitrov, Y. Chen, J. B. Sibarita, M. Bornens, *Proc. Natl. Acad. Sci. U. S. A.* **2006**, *103*, 19771.
- [14] J. M. Goffin, P. Pittet, G. Csucs, J. W. Lussi, J. J. Meister, B. Hinz, *J. Cell Biol.* **2006**, *172*, 259.
- [15] F. T. Bosman, I. Stamenkovic, *J. Pathol.* **2003**, *200*, 423.
- [16] E. A. Clark, J. S. Brugge, *Science* **1995**, *268*, 233.
- [17] Y. Q. Liu, D. R. Senger, *FASEB J.* **2004**, *18*, 457.
- [18] A. Bernard, J. P. Renault, B. Michel, H. R. Bosshard, E. Delamarche, *Adv. Mater.* **2000**, *12*, 1067.
- [19] D. T. Chiu, N. L. Jeon, S. Huang, R. S. Kane, C. J. Wargo, I. S. Choi, D. E. Ingber, G. M. Whitesides, *Proc. Natl. Acad. Sci. USA* **2000**, *97*, 2408.
- [20] J. Tien, C. M. Nelson, C. S. Chen, *Proc. Natl. Acad. Sci. USA* **2002**, *99*, 1758.
- [21] W. S. Yeo, M. Mrksich, *Langmuir* **2006**, *22*, 10816.
- [22] D. Ryan, B. A. Parviz, V. Linder, V. Semetey, S. K. Sia, J. Su, M. Mrksich, G. M. Whitesides, *Langmuir* **2004**, *20*, 9080.
- [23] Z. P. Yang, W. Frey, T. Oliver, A. Chilkoti, *Langmuir* **2000**, *16*, 1751.
- [24] A. L. Hook, N. H. Voelcker, H. Thissen, *Acta Biomater.* **2009**, *5*, 2350.
- [25] L. M. Demers, D. S. Ginger, S. J. Park, Z. Li, S. W. Chung, C. A. Mirkin, *Science* **2002**, *296*, 1836.
- [26] K. Takehara, S. Yamada, Y. Ide, *J. Electroanal. Chem.* **1992**, *333*, 339.
- [27] M. R. Shadnam, S. E. Kirkwood, R. Fedosejevs, A. Amirfazli, *Langmuir* **2004**, *20*, 2667.
- [28] D. Rhinow, N. A. Hampp, *IEEE Trans. Nanobiosci.* **2006**, *5*, 188.
- [29] S. Meyyappan, M. R. Shadnam, A. Amirfazli, *Langmuir* **2008**, *24*, 2892.
- [30] D. Rhinow, N. A. Hampp, *Adv. Mater.* **2007**, *19*, 1967.
- [31] L. Iversen, O. Younes-Metzler, K. L. Martinez, D. Stamou, *Langmuir* **2009**, *25*, 12819.
- [32] I. Doron-Mor, Z. Barkay, N. Filip-Granit, A. Vaskevich, I. Rubinstein, *Chem. Mat.* **2004**, *16*, 3476.
- [33] E. Xenogiannopoulou, K. Iliopoulos, S. Couris, T. Karakouz, A. Vaskevich, I. Rubinstein, *Adv. Funct. Mater.* **2008**, *18*, 1281.
- [34] B. Feng, Z. X. Li, X. Zhang, *Thin Solid Films* **2009**, *517*, 2803.
- [35] M. R. Shadnam, S. E. Kirkwood, R. Fedosejevs, A. Amirfazli, *J. Phys. Chem. B* **2005**, *109*, 11996.
- [36] K. von der Mark, J. Park, S. Bauer, P. Schmuki, *Cell Tissue Res.* **2010**, *339*, 131.
- [37] J. B. Schlenoff, M. Li, H. Ly, *J. Am. Chem. Soc.* **1995**, *117*, 12528.
- [38] X. Zhang, S. S. Chu, J. R. Ho, C. P. Grigoropoulos, *Appl. Phys. A: Mater. Sci. Proc.* **1997**, *64*, 545.
- [39] R. Kelly, J. J. Cuomo, P. A. Leary, J. E. Rothenberg, B. E. Braren, C. F. Aliotta, *Nucl. Instrum. Methods Phys. Res. Sect. B-Beam Interact. Mater. Atoms* **1985**, *9*, 329.
- [40] R. O. Hynes, *Cell* **1992**, *69*, 11.
- [41] R. Zaidel-Bar, M. Cohen, L. Addadi, B. Geiger, *Biochem. Soc. Trans.* **2004**, *32*, 416.
- [42] A. Y. Alexandrova, K. Arnold, S. Schaub, J. M. Vasiliev, J. J. Meister, A. D. Bershadsky, A. B. Verkhovsky, *PLoS One* **2008**, *3*, 9.
- [43] C. K. Choi, M. Vicente-Manzanares, J. Zareno, L. A. Whitmore, A. Mogilner, A. R. Horwitz, *Nat. Cell Biol.* **2008**, *10*, 1039.
- [44] R. Zaidel-Bar, S. Itzkovitz, A. Ma'ayan, R. Iyengar, B. Geiger, *Nat. Cell Biol.* **2007**, *9*, 858.
- [45] J. H. Slater, W. Frey, *J. Biomed. Mater. Res. Part A* **2008**, *87A*, 176.
- [46] N. Hartmann, T. Balgar, R. Bautista, S. Franzka, *Surf. Sci.* **2006**, *600*, 4034.
- [47] T. Balgar, S. Franzka, N. Hartmann, *Applied Phys. A: Mater. Sci. Proc.* **2006**, *82*, 689.
- [48] D. J. Ehrlich, J. Y. Tsao, *Appl. Phys. Lett.* **1984**, *44*, 267.
- [49] B. Klingebiel, L. Scheres, S. Franzka, H. Zuilhof, N. Hartmann, *Langmuir* **2010**, *26*, 6826.
- [50] T. Balgar, S. Franzka, N. Hartmann, E. Hasselbrink, *Langmuir* **2004**, *20*, 3525.
- [51] N. Garg, E. Carrasquillo-Molina, T. R. Lee, *Langmuir* **2002**, *18*, 2717.
- [52] B. M. Lamb, S. Park, M. N. Yousaf, *Langmuir* **2010**, *26*, 12817.
- [53] J. T. Smith, J. K. Tomfohr, M. C. Wells, T. P. Beebe, T. B. Kepler, W. M. Reichert, *Langmuir* **2004**, *20*, 8279.
- [54] C. A. Reinhart-King, M. Dembo, D. A. Hammer, *Biophys. J.* **2005**, *89*, 676.
- [55] P. Rajagopalan, W. A. Marganski, X. Q. Brown, J. Y. Wong, *Biophys. J.* **2004**, *87*, 2818.
- [56] C. Gaudet, W. A. Marganski, S. Kim, C. T. Brown, V. Gunderia, M. Dembo, J. Y. Wong, *Biophys. J.* **2003**, *85*, 3329.
- [57] M. H. Lee, P. Ducheyne, L. Lynch, D. Boettiger, R. J. Composto, *Biomaterials* **2006**, *27*, 1907.
- [58] B. T. Houseman, M. Mrksich, *Biomaterials* **2001**, *22*, 943.
- [59] L. Y. Li, S. F. Chen, J. Zheng, B. D. Ratner, S. Y. Jiang, *J. Phys. Chem. B* **2005**, *109*, 2934.
- [60] K. L. Prime, G. M. Whitesides, *J. Am. Chem. Soc.* **1993**, *115*, 10714.
- [61] B. Zhu, T. Eurell, R. Gunawan, D. Leckband, *J. Biomed. Mater. Res.* **2001**, *56*, 406.
- [62] E. Palin, H. N. Liu, T. J. Webster, *Nanotechnology* **2005**, *16*, 1828.
- [63] K. L. Elias, R. L. Price, T. J. Webster, *Biomaterials* **2002**, *23*, 3279.
- [64] M. J. Dalby, D. Giannaras, M. O. Riehle, N. Gadegaard, S. Affrossman, A. S. G. Curtis, *Biomaterials* **2004**, *25*, 77.
- [65] D. C. Miller, K. M. Haberstroh, T. J. Webster, *J. Biomed. Mater. Res. Part A* **2005**, *73A*, 476.
- [66] J. S. Miller, M. I. Bethencourt, M. Hahn, T. R. Lee, J. L. West, *Bio-technol. Bioeng.* **2006**, *93*, 1060.

Copyright WILEY-VCH Verlag GmbH & Co. KGaA, 69469 Weinheim, Germany, 2011

ADVANCED FUNCTIONAL MATERIALS

Supporting Information

for *Adv. Funct. Mater.*, DOI: 10.1002/adfm.201100297

Fabrication of Multifaceted Micropatterned Surfaces with
Laser Scanning Lithography

John H. Slater, Jordan S. Miller, Shann S. Yu, and Jennifer L.
West*

“Fabrication of Multifaceted Micropatterned Surfaces with Laser Scanning Lithography”
 By John H. Slater, Jordan S. Miller, Shann S. Yu, & Jennifer L. West*

Supporting Information

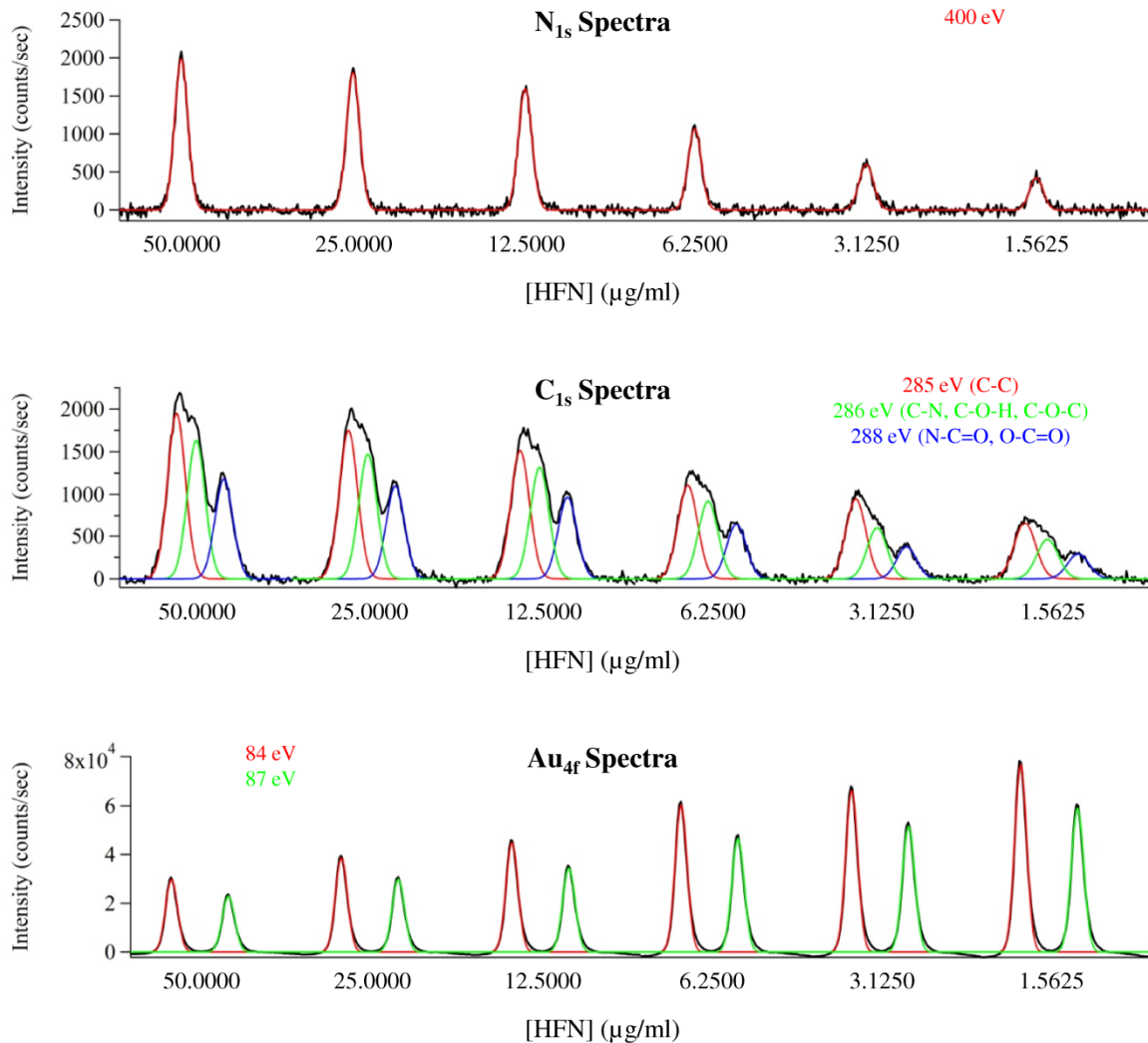


Figure S1: XPS Spectra of HFN Adsorbed to Au at Varying Concentrations

Au films were exposed to varying concentrations of HFN in solution ($50.0\text{-}1.5625 \mu\text{g ml}^{-1}$) for 30 mins at 37°C , rinsed with PBS, rinsed with MPH₂O, dried with N₂, and examined with high-resolution XPS. The raw spectra (black data) was deconvoluted with Gaussian fits (colored data) to examine the bond types present and to determine the contribution of each bond type to the elemental spectra. The legend for each spectra indicates the peak position of the Gaussian fits and is color coded to match the data. The data indicates that less HFN adsorbed to the surface as the solution concentration decreased. Both the N_{1s} and C_{1s} signal intensities steadily decreased with decreased HFN concentration. Concurrently, the Au_{4f} signal intensity increased from a reduction in shadowing of the Au background as less HFN adsorbed to the surface. The HFN surface density at each solution concentration displayed in Fig. 8A was determined through

quantification of the area under the N_{1s} peaks shown above. See Table S1 for quantification of the data above.

HFN [$\mu\text{g ml}^{-1}$]	Composition [%]			C _{1s} Deconvolution [%]			N _{1s} Area [AU]	HFN Density [# μm^{-2}]	RGD Density [# μm^{-2}]
	C _{1s}	N _{1s}	Au _{4f}	285 eV	286 eV	288 eV			
50	63.69	16.98	19.33	40.93	34.26	24.81	3202 \pm 84	2500 \pm 66	5000 \pm 131
25	58.77	15.72	25.51	40.49	34.06	25.45	2942 \pm 111	2297 \pm 87	4593 \pm 173
12.5	55.22	14.04	30.74	39.80	34.70	25.50	2630 \pm 130	2053 \pm 102	4106 \pm 203
6.25	45.26	9.63	45.12	41.50	34.51	23.99	2119 \pm 412	1654 \pm 322	3309 \pm 644
3.125	37.01	6.18	56.81	49.34	31.10	19.56	1160 \pm 186	905 \pm 145	1811 \pm 290
1.5625	30.03	4.24	65.73	46.68	32.67	20.65	617 \pm 166	481 \pm 129	963 \pm 258

Table S1: XPS Analysis of HFN Adsorbed to Au at Varying Concentrations

The spectra displayed in Fig. S1 was analyzed to determine the elemental composition, bond types present in the C_{1s} spectra, area under the N_{1s} peak, HFN surface density, and RGD surface density for each concentration of HFN. The HFN surface density was estimated by setting the saturation level to a previously published value of fibronectin saturation and by using the N_{1s} peak areas to ratiometrically back calculate the HFN surface density for the other surfaces. The RGD surface density was estimated by multiplying the HFN surface density by a factor of two; the number of RGD domains per HFN molecule.

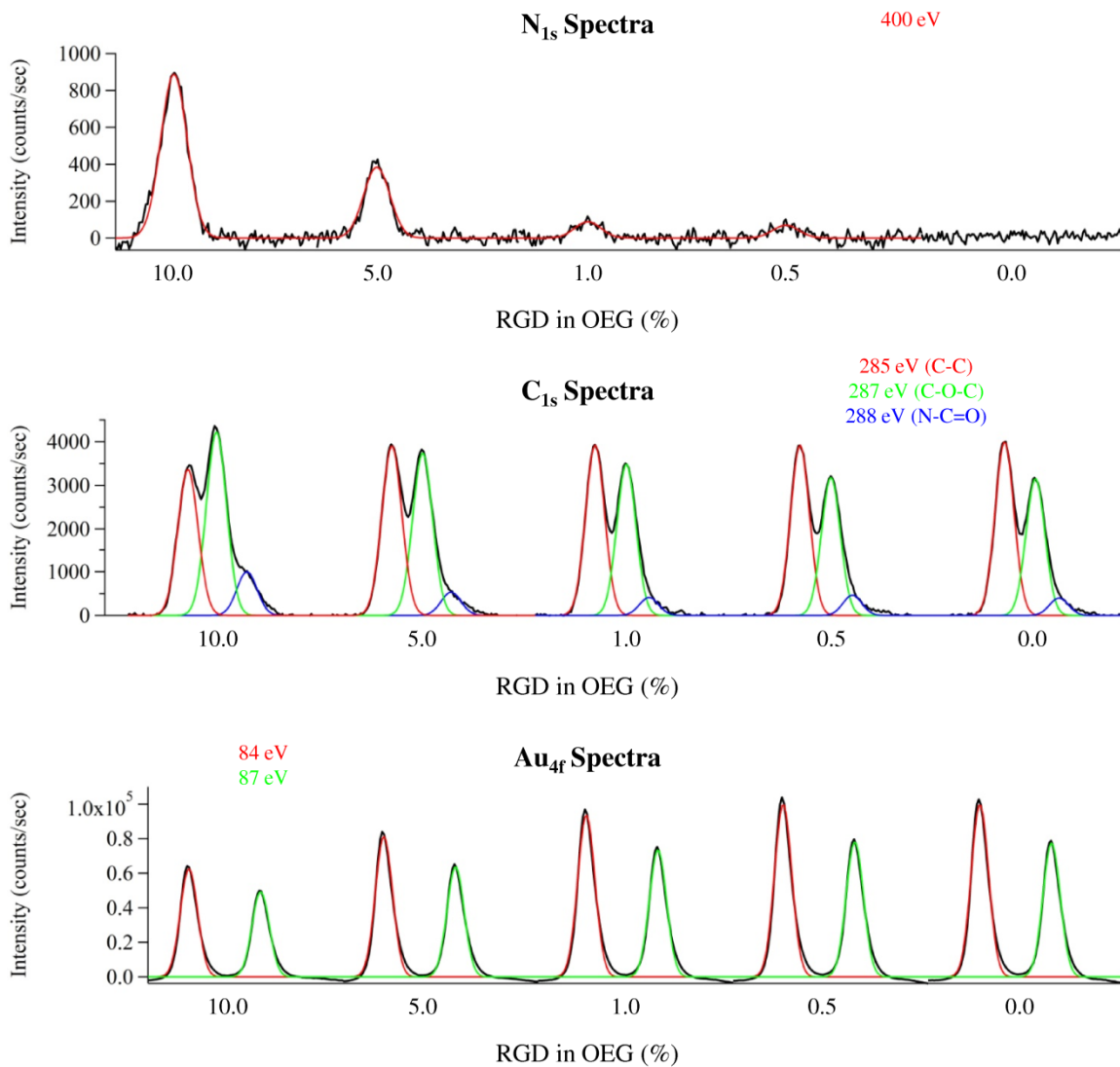


Figure S2: XPS Spectra of Mixed GRGD/OEG₃ SAMs on Au at Varying GRGD Percentages

Au films were functionalized with a mixed thiol solution (2 mM for 1 hr) of GRGD- and OEG₃-terminated alkanethiols with the percent GRGD varied from 10-0% (for example, the 10% GRGD solution was comprised of equal volumes of 0.2 mM GRGD-terminated and 1.8 mM OEG₃-terminated alkanethiols). The samples were rinsed thoroughly with ethanol, dried with N₂, and examined with high-resolution XPS. The raw spectra (black data) was deconvolved with Gaussian fits (colored data) to examine the bond types present and to determine the contribution of each bond type to the elemental spectra. The legend for each spectra indicates the peak position of the Gaussian fits and is color coded to match the data. The results indicate a reduction in the number of amide bonds present on the surface as the percent GRGD in solution decreased. The N_{1s} signal intensity (400 eV) and the amide bond contribution to the C_{1s} spectra (288 eV) steadily decreased as the percent GRGD in solution was reduced. It should be noted that the sensitivity factor for N_{1s} electrons is higher than that of C_{1s} electrons and therefore the N_{1s} spectra was used to characterize the RGD surface density shown in Fig. 8B. Another indicator that less GRGD-terminated thiol bound to the surface with decreasing percent GRGD was

observed by examining the contribution of the EG spacer to the C_{1s} spectra at 287 eV. The GRGD-terminated alkanethiol contained an EG₆ spacer between the alkyl chain and peptide while the OEG₃-terminated alkanethiol contained a shorter EG₃ terminal group, therefore as the percent GRGD was reduced the contribution of the EG signal to the C_{1s} spectra steadily decreased. Concurrently, an increase in the Au_{4f} background signal was observed with decreased percent GRGD as shadowing of the Au was reduced as the EG₆ surface concentration dropped and the EG₃ concentration increased. See Table S2 for quantification of the data above.

GRGD in OEG [%]	Elemental Composition [%]				C _{1s} Deconvolution [%]			N _{1s} Area [AU]	RGD Density [# μm ⁻²]
	C _{1s}	N _{1s}	O _{1s}	Au _{4f}	285 eV	287 eV	288 eV		
10.0	57.67	5.14	11.51	25.69	39.33	49.44	11.23	1736 ± 19	481813 ± 5274
5.0	57.34	0.76	6.86	35.05	47.29	46.15	6.56	640 ± 165	177581 ± 45884
1.0	52.19	0.74	6.19	40.89	50.25	44.83	4.92	163 ± 17	45165 ± 4733
0.5	51.22	1.00	3.20	44.59	51.92	42.64	5.44	118 ± 28	32809 ± 7704
0	51.95	0.00	4.24	43.81	53.10	41.20	5.70	0 ± 0	0 ± 0

Table S2: XPS Analysis of Mixed GRGD/OEG₃ SAMs on Au at Varying GRGD Percentages

The spectra displayed in Fig. S2 was analyzed to determine the elemental composition, bond types present in the C_{1s} spectra, area under the N_{1s} peak, and RGD surface density for each percentage of GRGD. The RGD surface density for each surface was estimated by setting the density of the 1% GRGD surface to a previously published value and by using the N_{1s} peak areas to ratiometrically back calculate the RGD density for the other surfaces.

20x (NA0.8) Objective						
λ [nm]	Power [%]	Power [mW]	Airy Disk [nm]	Intensity [mW μm ⁻²]	D _t [μsec]	Fluence [nJ μm ⁻²]
532	100	4.11	811	7.95	0.95	7.55
532	100	4.11	811	7.95	1.61	12.80
532	100	4.11	811	7.95	2.56	20.35
532	100	4.11	811	7.95	3.20	25.44
532	100	4.11	811	7.95	6.39	50.80
532	80	3.2	811	6.19	0.95	5.88
532	80	3.2	811	6.19	1.61	9.97
532	80	3.2	811	6.19	2.56	15.85
532	80	3.2	811	6.19	3.20	19.81
532	80	3.2	811	6.19	6.39	39.55

Table S3: Laser Properties Used for LSL with a 20x (NA0.8) Air Objective

A 532 nm laser was focused through a 20x (NA0.8) air objective. The power of the focused laser beam was measured at the focal plane of the objective. The Airy Disk was calculated based on the wavelength and NA of the objective and used to estimate the laser intensity. The pixel dwell time was varied from 0.95-6.39 μsec and the corresponding laser fluence was calculated.

63x (NA1.4) Objective

λ [nm]	Power [%]	Power [mW]	Airy Disk [nm]	Intensity [mW μm^{-2}]	D_t [μsec]	Fluence [nJ μm^{-2}]
532	100	3.50	464	20.73	0.95	19.70
532	100	3.50	464	20.73	1.61	33.38
532	100	3.50	464	20.73	2.56	53.08
532	100	3.50	464	20.73	3.20	66.35
532	100	3.50	464	20.73	6.39	132.49
532	80	3.00	464	17.77	0.95	16.88
532	80	3.00	464	17.77	1.61	28.61
532	80	3.00	464	17.77	2.56	45.50
532	80	3.00	464	17.77	3.20	56.87
532	80	3.00	464	17.77	6.39	113.57

Table S4: Laser Properties Used for LSL with a 63x (NA1.4) Oil Immersion Objective

A 532 nm laser was focused through a 63x (NA1.4) oil immersion objective. The power of the focused laser beam was measured at the focal plane of the objective. The Airy Disk was calculated based on the wavelength and NA of the objective and used to estimate the laser intensity. The pixel dwell time was varied from 0.95-6.39 μsec and the corresponding laser fluence was calculated.